JEM Journal of Experimental Medicine

ARTICLE

CD16⁺CD163⁺ monocytes traffic to sites of inflammation during necrotizing enterocolitis in premature infants

Oluwabunmi O. Olaloye[1*], Peng Liu[2*], Jessica M. Toothaker[3], Blake T. McCourt[1], Collin C. McCourt[4], Jenny Xiao[5], Erica Prochaska[6], Spenser Shaffer[7], Lael Werner[8,9], UPMC NICU Faculty[7], UPMC Pediatric Surgery Faculty[10], Jordan Gringauz[11], Misty Good[12], Jeffrey D. Goldsmith[13], Xiaojing An[14], Fujing Wang[14], Scott B. Snapper[15], Dror Shouval[8,9], Kong Chen[14], George Tseng[2], and Liza Konnikova[1,3,7,16,17]

Necrotizing enterocolitis (NEC) is a severe gastrointestinal complication of prematurity. Using suspension and imaging mass cytometry coupled with single-cell RNA sequencing, we demonstrate severe inflammation in patients with NEC. NEC mucosa could be subtyped by an influx of three distinct neutrophil phenotypes (immature, newly emigrated, and aged). Furthermore, CD16⁺CD163⁺ monocytes/Mϕ, correlated with newly emigrated neutrophils, were specifically enriched in NEC mucosa, found adjacent to the blood vessels, and increased in circulation of infants with surgical NEC, suggesting trafficking from the periphery to areas of inflammation. NEC-specific monocytes/Mϕ transcribed inflammatory genes, including TREM1, IL1A, IL1B, and calprotectin, and neutrophil recruitment genes IL8, CXCL1, CXCL2, CXCL5 and had enrichment of gene sets in pathways involved in chemotaxis, migration, phagocytosis, and reactive oxygen species generation. In summary, we identify a novel subtype of inflammatory monocytes/Mϕ associated with NEC that should be further evaluated as a potential biomarker of surgical NEC and a target for the development of NEC-specific therapeutics.

Introduction

Preterm births account for 10% of all pregnancies in the United States, equaling 500,000 infants per year (Purisch and Gyamfi-Bannerman, 2017). Premature delivery is associated with significant morbidity and mortality and is the leading cause of death in children under 5 (Liu et al., 2012; Purisch and Gyamfi-Bannerman, 2017). Necrotizing enterocolitis (NEC) is a devastating gastrointestinal complication of prematurity, with high morbidity, mortality, and economic burden (Patel et al., 2015; Houben et al., 2017; Neu and Walker, 2011). It occurs in 1–7% of all premature infants in the first 2–6 wks of life, with a peak incidence between 29 and 32 wks corrected gestational age (GA; Patel et al., 2015; Yee et al., 2012). Despite that survival and long-term outcomes have improved overall for premature infants, the rate of death from NEC has only increased. No NEC-specific therapy exists (Ellsbury et al., 2016; Holman et al., 2006; Guillet et al., 2006), and with the current care, 20–30% of infants with NEC die. Those who survive will face numerous short-term and long-term problems, including intestinal complications, poor growth, and neurodevelopmental delays (Jones and Hall, 2020). As such, there is a dire need to improve our understanding of NEC pathogenesis to determine specific biomarkers and targeted therapeutics.

NEC is known to be a multifactorial disease, but its pathogenesis remains incompletely understood. Prematurity, intestinal dysbiosis, and impaired immune defenses have all been implicated in NEC pathogenesis (Neu and Pammi, 2017; Denning

[1]Department of Pediatrics, Yale Medical School, New Haven, CT; [2]Department of Biostatistics, University of Pittsburgh, Pittsburgh, PA; [3]Department of Immunology, University of Pittsburgh, Pittsburgh, PA; [4]Department of Pediatrics, University of Pittsburgh Medical Center, Children's Hospital of Pittsburgh, Pittsburgh, PA; [5]Department of Biology, University of Pittsburgh, Pittsburgh, PA; [6]Division of Infectious Diseases, Department of Pediatrics, Johns Hopkins University School of Medicine, Baltimore, MD; [7]Division of Newborn Medicine, University of Pittsburgh Medical Center, Children's Hospital of Pittsburgh, Pittsburgh, PA; [8]Institute of Gastroenterology, Nutrition and Liver Disease, Schneider Children's Medical Center of Israel, Petah Tiqwa, Israel; [9]Sackler Faculty of Medicine, Tel Aviv University, Tel Aviv, Israel; [10]Division of Pediatric Surgery, Department of Surgery, University of Pittsburgh Medical Center, Children's Hospital of Pittsburgh, Pittsburgh, PA; [11]Department of Medicine, Boston Children's Hospital, Boston, MA; [12]Department of Pediatrics, Washington University School of Medicine, St. Louis, MO; [13]Department of Pathology, Boston Children's Hospital, Boston, MA; [14]Department of Medicine, University of Pittsburgh Medical Center Montefiore Hospital, Pittsburgh, PA; [15]Division of Gastroenterology, Hepatology and Nutrition, Boston Children's Hospital, Boston, MA; [16]Division of Reproductive Sciences, Yale University, New Haven, CT; [17]Program in Human and Translational Immunology Yale University, New Haven, CT.

*O.O. Olaloye and P. Liu contributed equally to this paper; Correspondence to Liza Konnikova: liza.konnikova@yale.edu.

et al., 2017; Chen et al., 2016b). Previous studies have identified a number of cell types involved in the immune dysregulation characteristic of NEC. These include an increase in intestinal monocytes and neutrophils and a decrease in regulatory T cells (T reg cells; Weitkamp et al., 2013; Weitkamp et al., 2014; Managlia et al., 2019; Pang et al., 2018b). Furthermore, recent studies have implicated TLR signaling and T helper 17 cells, a subtype of T cells, in the pathogenesis of NEC (Egan et al., 2015). However, more detailed phenotypic and functional analysis, permitted by the state-of-the-art single-cell techniques that would allow for a much more nuanced understanding of the immune dysregulation in NEC, has not been performed.

Susceptibility to inflammatory/infectious diseases in newborns was thought to be based on tolerance required to prevent fetal rejection in utero (Jennewein et al., 2017; Hobbs and Davis, 1967). Newborns were postulated to rely on passive immunity via maternal transfer of IgG in the third trimester (Jennewein et al., 2017), and as such, premature infants delivered before the third trimester were thought to be at higher risk of infections compared with term infants. This paradigm has recently been challenged. New findings suggest that preterm infants born as early as 24 wks GA have similar IgG repertoires as term infants (Pou et al., 2019). Additionally, fetal mucosal immunity is established early in utero (Schreurs et al., 2019; Stras et al., 2019; Li et al., 2019). Taken together, these findings suggest that increased susceptibility to inflammation in preterm neonates is unlikely due to immaturity alone and rather stems from underlying defects in immune maturation and/or regulation. We hypothesize that infants who develop NEC have disease-specific immune defects and propose that simultaneous single-cell analysis of intestinal tissue and peripheral blood of infants diagnosed with NEC will shed light on its pathogenesis and provide useful biomarkers and targets for new drug development.

One of the challenges to studying NEC has been identifying appropriate controls for comparison as intestinal tissue from healthy, age-matched subjects is ethically unattainable. As such, more readily available samples are needed as surrogates. However, it is unclear which of these would serve as optimal controls. Recent evidence (Stras et al., 2019; Schreurs et al., 2019; Li et al., 2019) has suggested that the fetal intestinal immune system is largely developed; thus, fetal tissue would serve as a reasonable alternative. However, it is challenging to procure and lacks abundant microbial exposure. Another alternative is neonatal tissue obtained from non–NEC-related surgeries. However, these typically come from full-term rather than premature infants. Finally, preterm infants with localized spontaneous intestinal perforation (SIP; another intestinal complication of prematurity thought to have a distinct pathophysiology from NEC) would be GA matched to NEC cases but likely have other confounding factors that predisposed them to SIP. To overcome these limitations, in the current study (total n = 34; Table S1 A), we have compared the mucosal immune landscape of the small intestine of infants with NEC with samples obtained from fetal, SIP, neonatal, and post-NEC cases simultaneously. We further supplemented our analysis with blood obtained from infants treated for NEC and chronologic and GA-matched control subjects (total n = 28; Table S1 B) In the present study, using a combination of multiomic techniques, including deep immunophenotyping via mass cytometry by time of flight (CyTOF), functional analysis via single-cell RNA sequencing (scRNA-seq), and anatomical localization with imaging mass cytometry (IMC) of small intestinal mucosa, we describe severe immune dysregulation in NEC and identify a population of highly inflammatory CD16$^+$CD163$^+$ monocytes that traffic from the periphery and are involved in the pathogenesis of NEC.

Results

In the following studies, we used multiomic techniques to define mucosal and peripheral immune disturbances in patients with NEC. Using a suspension mass cytometry, CyTOF (Table S2), we explored immune cells from cryopreserved small intestinal mucosal samples in a cohort of neonates with NEC (n = 12); tissue at reanastomosis surgery in infants with a previous diagnosis of NEC (postNEC n = 4); and control subjects without a history of NEC, as follows: (a) second trimester fetal cases (fetal, n = 3), (b) neonates with SIP (SIP, n = 8), and (c) neonates with nonimmune gastrointestinal disorders (neonatal, n = 4; Fig. 1, A and B; Table S1, A and B; and Table S2). Data were clustered using an automated clustering algorithm, PhenoGraph, and analyzed to determine immune population and marker expression differences among the groups.

To determine anatomical localization and validate some of the key findings, formalin-fixed paraffin-embedded (FFPE) slides from a subset of neonatal (n = 3) and NEC (n = 6) samples studied with CyTOF were analyzed using IMC (Fig. 1, A and B; and Table S1 A). Furthermore, to complement the CyTOF findings, scRNA-seq was performed on a subset of small intestinal mucosa used for CyTOF (total n = 5) as outlined in Fig. 1, A and B, and Table S1 A.

Finally, intestinal data were supplemented with a cohort of patients with NEC, including two cases with matched small intestinal mucosa (total n = 15) and age-matched controls (n = 13) used for whole-blood studies (Table S1 B). Of note, we included two cases who initially served as healthy controls (analyzed as controls) developed NEC later on in their NICU stay.

Enrichment of neutrophil subtypes defines three distinct NEC phenotypes

Automated clustering of intestinal leukocytes (CD45$^+$; Fig. S1 A) identified 28 immune clusters (Fig. 1, C–E; and Fig. S1 B) that included neutrophils, monocytes/macrophages (Mϕ), non-Mϕ APCs, natural killer (NK) cells, innate lymphoid cells (ILCs), and T cells. Interestingly, each subject group was defined by a unique mucosal immune landscape (Fig. 1 F and Fig. S1 B).

Consistent with previous reports (Weitkamp et al., 2014; Hui et al., 2017), NEC was marked by global immune dysregulation (Fig. 1, E–G). Innate cells were increased in NEC cases compared with fetal and SIP cases (Fig. 1 G). To determine which innate cell type was driving the increase in total innate cells in the NEC samples, we evaluated the individual innate cell populations. An increase in total neutrophils (CD66b$^+$CD16$^+$) was evident in NEC compared with neonatal and fetal cases, with a similar trend to SIP cases (Fig. 1 H and Fig. S1 D).

To determine the phenotypes of neutrophils enriched in NEC, abundance and expression of markers of interest in five separate

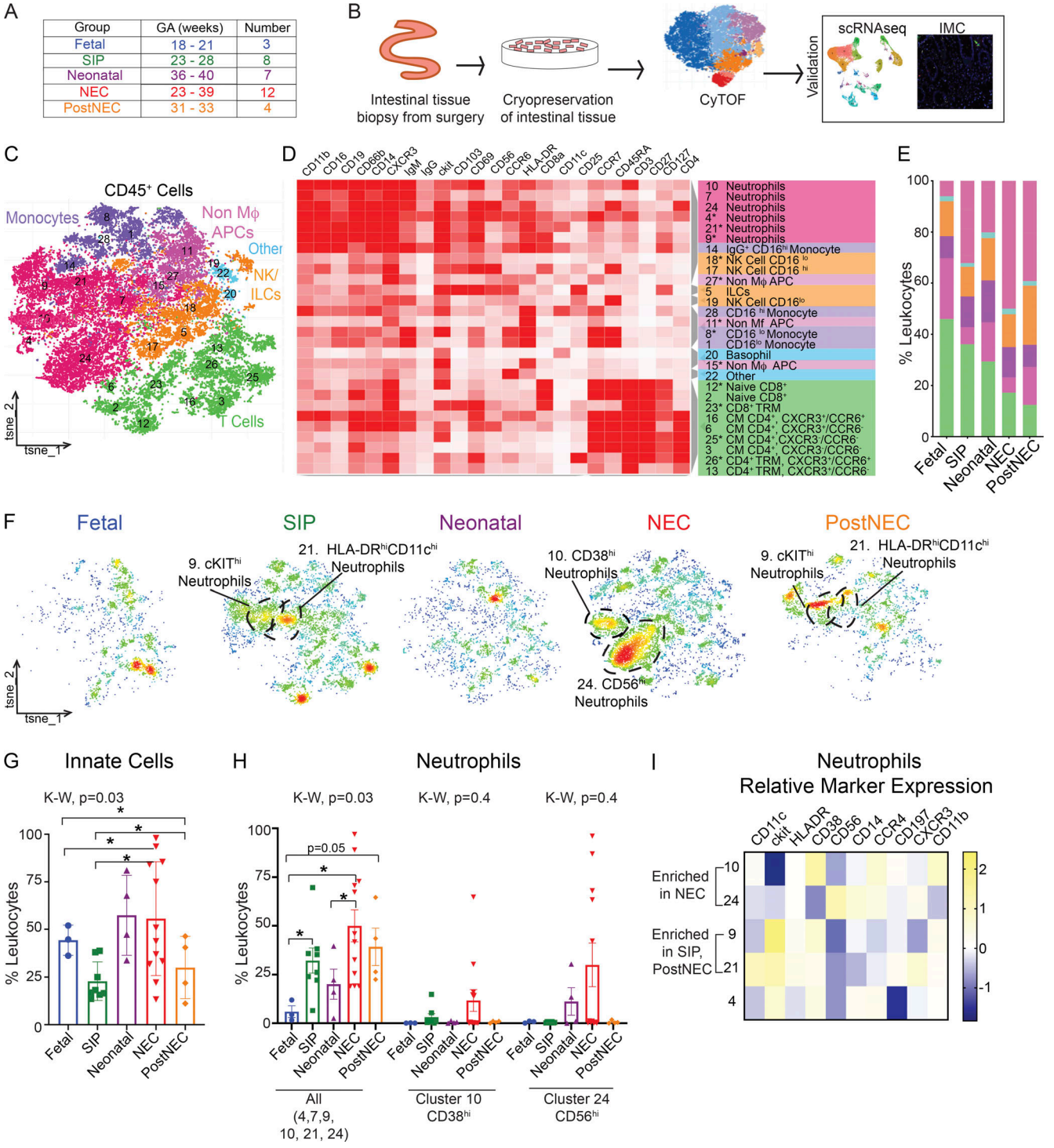

Figure 1. **Neutrophilic infiltrate defines distinct phenotypes in NEC mucosa. (A)** Table with number of cases in each group with GA range in weeks analyed with CyTOF, IMC, or scRNAseq. **(B)** Workflow of small intestinal mucosa analysis. **(C)** tSNE plot of CD45+ cells showing major populations, including monocytes, nonmonocyte APCs (Non Mϕ APCs), NK cells, ILCs, T cells, neutrophils, and others (cell types that we could not phenotype with the panel). **(D)** Heatmap of surface markers used to define populations in each cluster generated with clustergrammer (Fernandez et al., 2017). Asterisks denote clusters with significant differences among groups. **(E)** Median percentage of major populations color coded to correspond to the major populations in C and D. **(F)** Density tSNE plot of all leukocytes within each group, with abundant neutrophil clusters highlighted with dashed lines. **(G and H)** Abundance of innate cells (G) and all neutrophils (H) expressed as a percentage of leukocytes. **(I)** Relative expression of markers of interest in individual neutrophil clusters. Each dot represents one patient sample. Box plots represent mean ± SE. Groups are fetal (n = 3), SIP (n = 8), neonatal (n = 7), NEC (n = 12), and postNEC (n = 4). *, P < 0.05. K-W, Kruskal-Wallis test; Mϕ, macrophage.

neutrophil clusters (4, 9, 10, 21, 24) were compared. CCR4$^+$ CD38$^+$CD11b$^+$ (cluster 10) and CD56$^+$CXCR3$^+$ (cluster 24) neutrophils (Fig. 1, F and H) were enriched in NEC mucosa consistent with aged and newly infiltrating neutrophils, respectively. In contrast, cKIT$^+$ (cluster 9), immature neutrophils, and HLA-DR$^+$CD11c$^+$ (cluster 21) dendritic cell (DC)/neutrophil hybrids important in antigen presentation (Fites et al., 2018) were enriched in the SIP and postNEC cases (Fig. 1 H). Further analysis of the abundance of each neutrophil cluster revealed three distinct phenotypes of NEC (C9 NEC, C10 NEC, C24 NEC) based on which population of neutrophils (clusters 9, 10, 24, respectively) was enriched in the particular NEC cases, with C24 NEC being the most abundant (Fig. 1 H and I; and Fig. S1, D and E).

We performed Nanostring analysis of small intestine samples obtained from an independent cohort of patients to validate that neutrophil recruitment signatures are present in NEC samples (Table S1 B and Table S3). Consistent with the increase of infiltrating neutrophils in NEC, Nanostring analysis revealed that cytokines involved in recruiting neutrophils to the sites of inflammation, IL-6 and IL-8 (Bhatia et al., 2014; Wright et al., 2014), were indeed elevated in NEC tissue (Fig. S1 F). Furthermore, S100A8 and S100A9, both subunits of calprotectin, a marker of inflammation and a potent antimicrobial protein known to be derived from neutrophils and monocytes (Aydemir et al., 2012; MacQueen et al., 2016), were also elevated in NEC tissue (Fig. S1 F).

CD16$^+$CD163$^+$ monocytes uniquely enriched in NEC mucosa

To further define innate cell abnormalities associated with NEC, we reclustered the data solely on innate cells. CD66b$^+$ cells were excluded from the innate cell analysis given the high proportion of neutrophils in NEC that could obscure other findings. Analysis of CD3$^-$CD19$^-$CD66b$^-$ cells revealed 26 clusters (Fig. 2, A–C; and Fig. S1, G and H) with a disease-specific landscape in NEC samples (Fig. 2 D).

Among the APC populations, all CD103$^+$ DCs (clusters 10, 23, and 24) and CCR7$^+$CD103$^+$ DCs (clusters 10, 24) were reduced in NEC compared with fetal and SIP cases, with a similar trend compared with neonatal cases (Fig. S2 A). CCR7$^+$CD103$^+$ DCs are mature DCs critical for antigen presentation and recruitment of naive T cells to the intestine (Ruane and Lavelle, 2011), and a reduction in NEC suggests decreased or altered antigen presentation and T cell recruitment. They also play a critical role in maintaining tolerance to commensals and food antigens (Scott et al., 2011), and as such, their decrease could suggest a break in tolerance.

Examining the NK and ILC populations, CCR6$^+$CD16$^-$ NK cells (cluster 18) were reduced in NEC compared with both fetal and neonatal control samples (Fig. S2 B). However, ckit$^+$ ILCs (likely ILC3s) and tissue-resident (CD69$^+$CD103$^+$) ILCs were decreased in NEC compared with SIP and fetal samples (Fig. S2 C). These data indicate that perhaps the reduction in ILCs is secondary to increased chronologic age of NEC samples compared with fetal and SIP samples, while a decrease in NK cells is secondary to the underlying inflammation.

Focusing on monocytes/Mϕ, nonclassical (CD14^{lo}CD16$^+$) and intermediate (CD14$^+$CD16$^+$) monocytes were most abundant in NEC cases and significantly increased over the neonatal and fetal samples (Fig. 2 E). CD16$^+$ (low-affinity IgG receptor) monocytes bind to IgG and secrete proinflammatory cytokines (Narasimhan et al., 2019), and their overall increase in NEC suggests that NEC is characterized by an acute transient proinflammatory monocytic infiltrate. There were no differences in classical (CD14$^+$CD16$^-$) and anti-inflammatory (CD16$^-$CD163$^+$) monocytes among groups (Fig. 2 E). Consistent with this observation, as noted previously, Nanostring data revealed monocyte-associated cytokines IL-6, IL-8, IL-1β and its target gene TNFAIP3 (Swindell et al., 2018), and calprotectin (S100A8 and S100A9) to be upregulated in NEC compared with neonatal cases (Fig. S1 F). An intriguing population of CD16$^+$CD163$^+$ monocytes/Mϕ (clusters 1, 14, 21) were specifically enhanced in NEC above all other groups (Fig. 2 E). These dual-expressing monocytes also expressed HLA-DR in all three clusters (Fig. 2 B), and expression of CXCR5 (chemokine receptor, increased in M1 Mϕ; Xuan et al., 2015) and CD64 (high-affinity IgG receptor, similarly enhanced on M1 Mϕ; Hristodorov et al., 2015) was high in clusters 14 and 21 (Fig. 2 F).

To determine whether there was a correlation between neutrophil phenotypes and particular monocyte/Mϕ subtypes, we evaluated the abundance of monocyte populations in each of the three NEC subgroups identified by the subtype of neutrophil enrichment (immature/C9, aged/C10, and newly infiltrating/C24). This analysis revealed distinct differences within the three NEC phenotypes. Samples in the C24 NEC subgroup enriched for the CD56$^+$, newly infiltrating neutrophils (Hartl et al., 2008) were also enhanced for all monocytes/Mϕ, CD16$^+$ intermediate/nonclassical monocytes/Mϕ, and NEC-enriched CD16$^+$CD163$^+$ monocytes/Mϕ (Fig. 2 G). In particular, cluster 1, CD16$^+$CD163$^+$ monocytes/Mϕ were significantly enriched in the C24 NEC phenotype (Fig. 2 H). This highlights that monocyte/Mϕ, and specifically CD16$^+$CD163$^+$ monocytes/Mϕ, abundance is correlated with the CD56$^+$ neutrophils (cluster 24).

Peripheral neutropenia defines surgical NEC cases

Given that NEC mucosa was enriched for both cytokines known to recruit neutrophils and neutrophils themselves, we postulated that neutrophils that dominated the NEC mucosa have recently migrated from the periphery. To confirm this hypothesis and determine whether there were other immune abnormalities in patients with NEC, we recruited a cohort of patients with NEC and control subjects (Table S1). Using CyTOF, we analyzed circulating immune cells from whole blood (~100 µl) obtained during treatment for medical NEC (mNEC, n = 12) and surgical NEC (sNEC, n = 3) as well as from non-NEC GA-matched controls (n = 15; Fig. 3, A–E; and Table S1 B). Of note, two of the sNEC samples had both blood and small intestinal tissue analyzed.

Analysis of all leukocytes (CD45$^+$) revealed no major differences between control and NEC groups when medical and surgical NEC groups were combined (Fig. S2, D–H). Overall, infants with mNEC had a similar innate immune profile to healthy controls (Fig. 3 E). However, circulatory neutrophils were decreased in sNEC compared with mNEC and controls (Fig. 3, E and F), complementary to increased neutrophils observed in NEC small intestine. Peripheral neutropenia (absolute neutrophil count <1,500)

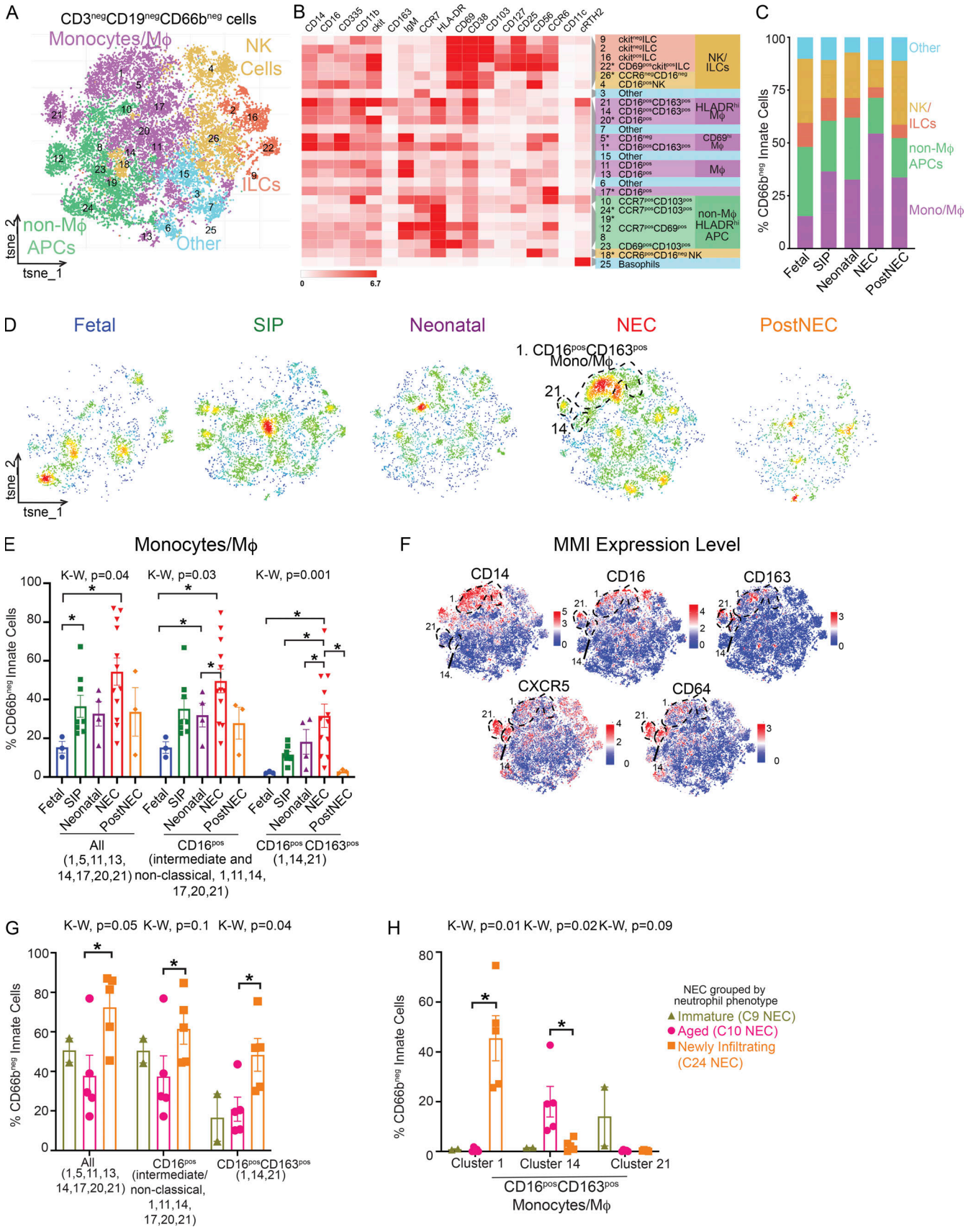

Figure 2. **Monocytes expressing CD16 and CD163 are enriched in NEC mucosa. (A)** tSNE plot of CD3⁻CD19⁻CD66b⁻ cells. **(B)** Clustergram (Fernandez et al., 2017) heatmap of canonical surface markers used to identify populations in each cluster; colors correspond to A. Asterisks denote clusters with significant

differences among groups. **(C)** Median percentage of major populations color coded to correspond to the major populations in A. **(D)** Density tSNE plots of $CD3^-CD19^-CD66b^-$ cells with $CD16^+CD163^+$ monocytes/Mϕ (clusters 1, 14, 21) highlighted in NEC. **(E)** Abundance of monocyte populations as a percentage of $CD66b^-$ innate cells among groups. **(F)** Mean metal intensity (MMI) expression of markers with increased expression in $CD16^+CD163^+$ monocytes/Mϕ (clusters 1, 14, 21). **(G and H)** Abundance of major monocyte/Mϕ populations (G) and individual $CD16^+CD163^+$ monocyte/Mϕ clusters (H) among NEC phenotypes/subgroups where immature/C9 NEC (n = 2), aged/C10 NEC (n = 5), and newly infiltrating C24 NEC (n = 5). Each dot represents one patient/sample. Box plots represent mean ± SE. Groups are fetal (n = 3), SIP (n = 8), neonatal (n = 7), NEC (n = 12), and postNEC (n = 4). C9 NEC, C10 NEC, and C24 NEC samples with abundance of $cKIT^+$, $CD38^{hi}$, and $CD56^{hi}$ neutrophils, respectively, as defined in Fig. S1. *, $P < 0.05$. K-W, Kruskal-Wallis test.

has been described in cases of severe NEC and associated with increased mortality (Hutter et al., 1976). Furthermore, there was an indirect correlation between total neutrophil abundance in the periphery and intestinal mucosa in the sNEC cases with matched blood and intestinal mucosa samples. The case with high intestinal neutrophils had low circulating neutrophils/neutropenia (Fig. S2 I).

Circulating $CD16^+CD163^+$ monocytes are found in infants with surgical NEC

Interestingly, we observed that $CD16^+CD163^+$ monocytes were increased in the circulation of sNEC patients (Fig. 3 G). Analysis of matched blood and tissue from the same patient to determine whether $CD16^+CD163^+$ monocytes traffic from the periphery to the site of inflammation was limited to only two cases. Nevertheless, for the two matched sNEC cases, there was a direct correlation between the abundance of $CD16^+CD163^+$ monocytes in blood and tissue, with surgical NEC case 1 having low abundance of $CD16^+CD163^+$ monocytes and NEC case 2 having a high proportion of $CD16^+CD163^+$ monocytes in both circulation and tissue (Fig. S2 J). These results demonstrate that there is an overall increase in $CD16^+CD163^+$ monocytes both in the periphery and in the intestine of infants with surgical NEC, suggesting that they likely traffic from the circulation to sites of intestinal inflammation.

$CD16^+CD163^+$ monocytes cluster around blood vessels in the NEC small intestine

We performed IMC of FFPE sections to test our hypothesis that $CD16^+CD163^+$ monocytes migrate from the peripheral blood to sites of active inflammation in the small intestine. A subset of cases, neonatal (n = 3) and NEC (n = 6), matched to our suspension CyTOF analysis, were analyzed using a panel of validated antibodies (Table S2). Regions of interest with markers of interest (DNA1, pancytokeratin [panCK], smooth muscle actin [SMA], CD14, CD16, CD163, and HLA-DR) were visualized using histocat 1.7.6.1 (Schapiro et al., 2017). We confirmed abundance of $CD16^+CD163^+$ monocytes/Mϕ (Fig. 4, asterisks) with variable $HLA\text{-}DR^+$ expression in NEC tissue. Moreover, we were able to identify numerous $CD16^+CD163^+$ monocytes/Mϕ adjacent to a blood vessels (Fig. 4, dashes) in support of our hypothesis that they likely traffic from the periphery.

Numerous immune and nonimmune populations interact with $CD16^+CD163^+$ monocytes/Mϕ

Single-cell information, spatial features, and cell-to-cell interactions can be visualized and obtained from IMC data using the graphical user interface from histocat 1.7.6.1 (Schapiro et al., 2017). Using this algorithm, significant interactions between cell populations in unique environments can be determined within a cohort or across all images. To investigate what cell types are in communication with $CD16^+CD163^+$ monocytes/Mϕ in the NEC mucosa, we applied a recently published pipeline to determine neighboring populations with significantly enriched interactions (Damond et al., 2019). We then adapted the pipeline to our dataset using ilastik (Berg et al., 2019) and trained a random forest classifier to identify nucleus, membrane, and cytoplasm in small intestinal tissue (details in Materials and methods; Fig. 5 A).

IMC files and the trained cell mask were uploaded to histoCAT 1.7.6.1 (Schapiro et al., 2017) to run PhenoGraph analysis and to identify cell-to-cell interactions. Twenty-five unique clusters were identified (Fig. 5 B; and Fig. S3, A–C). Two clusters (phenographs 5 and 6) were $CD16^+CD163^+$ monocytes/Mϕ (Fig. 5, B–D; and Fig. S3, C–F). $CD16^+CD163^+$ monocytes/Mϕ were present in all layers of intestinal tissue in NEC, consistent with transmural inflammation (Fig. 5 F). Neighborhood analysis revealed that phenograph cluster 6 ($CD16^+CD163^+$ monocytes/Mϕ) was in proximity to a large number of cell types, including other monocytes/Mϕ (clusters 5, 13, 20, and 22), B cells (cluster 24), T cells (clusters 16 and 23), unidentified immune cells (cluster 7), SMA^+ cells (clusters 12 and 19), and nonimmune cells (cluster 15; Fig. 5, E and F; and Fig. S3 C). This reinforces the notion that $CD16^+CD163^+$ monocytes/Mϕ are enriched in NEC and likely play diverse functions in NEC mucosa, including regulating B cell responses and antigen presentation.

One of the strongest interactions was with cluster 5 cells that represent monocytes/Mϕ of similar phenotypes but with lower CD16 and CD163 expression, perhaps suggesting that both clusters represent the same monocytes in different states of activation (Fig. 5 F). Another strong interaction was with T reg cells (cluster 23), possibly representing an attempt by T reg cells to suppress $CD16^+CD163^+$ monocytes/Mϕ. Finally, $CD16^+CD163^+$ monocytes/Mϕ had enhanced interactions with SMA^+ cells (clusters 12 and 19), highlighting the transmural nature of inflammation associated with NEC. Unfortunately, our IMC panel did not include a specific endothelial marker, prohibiting us from bioinformatically confirming $CD16^+CD163^+$ monocyte/Mϕ proximity to the vasculature. Importantly, when stratifying the interactions by disease state, both clusters 5 and 6 had an increase in significant interactions in the NEC samples compared with neonatal samples (Fig. S3 G). Interactions with SMA^+, cluster 12; T reg cells, cluster 23; and B cells, cluster 24, were especially enriched in the NEC samples (Fig. S3 G). On the other hand, interactions of anti-inflammatory cell types such as T reg cells, cluster 23, and $CD163^+$ Mϕ, cluster 22, with other cell types (Fig. S3 G, black dashed box) were more prominent in neonatal samples.

scRNA-seq analysis confirms $CD16^+CD163^+$ Mϕ abundance in NEC tissue

To further probe the activation state, gene expression signatures, and functional phenotypes of monocytes in NEC tissue,

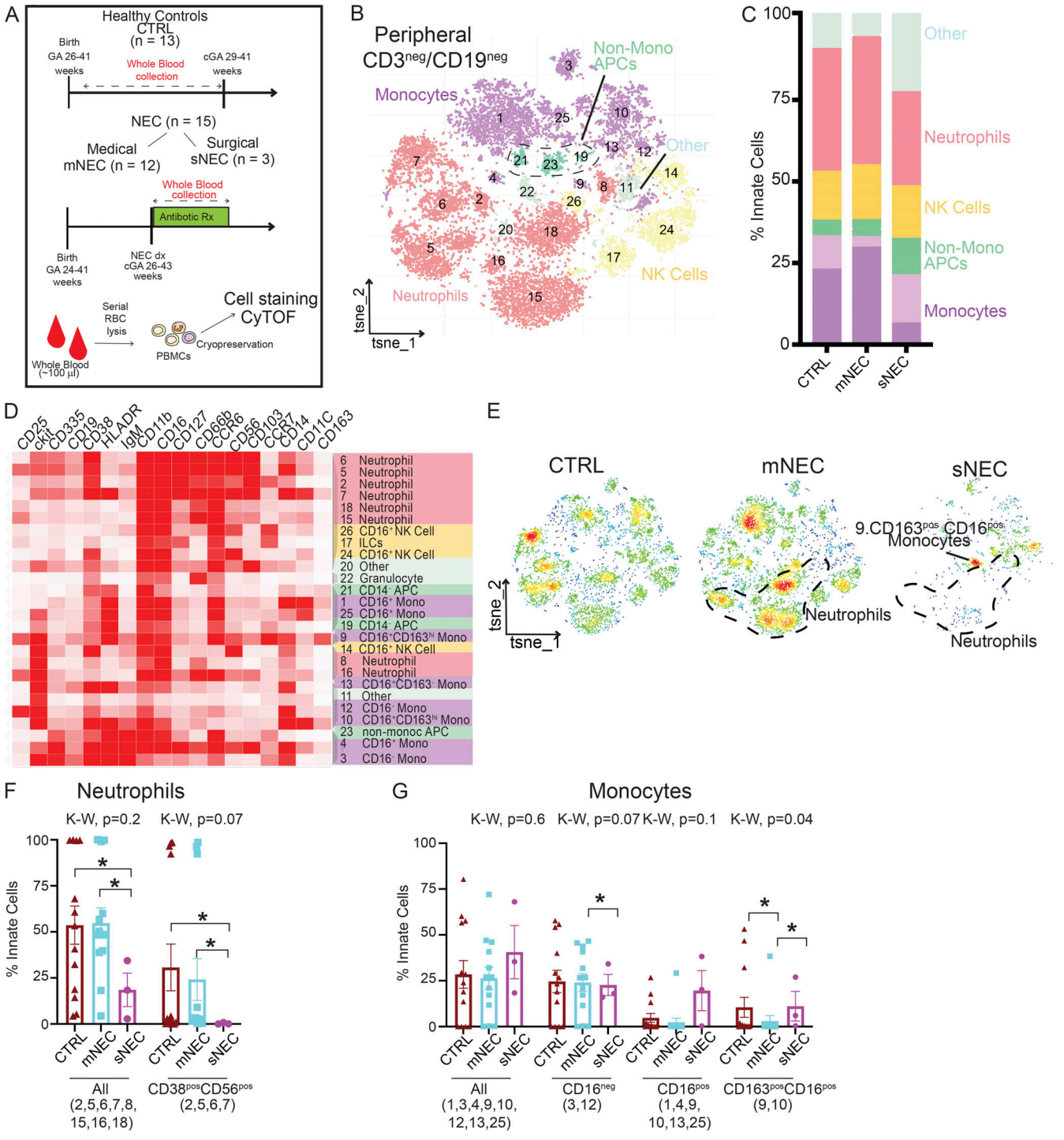

Figure 3. **Peripheral neutropenia and increase in CD16⁺CD163⁺ monocytes/Mϕ in infants with surgical NEC. (A)** Workflow for collection and analysis of peripheral blood. **(B)** tSNE of peripheral CD3⁻CD19⁻ innate cells. **(C)** Abundance of major populations expressed as a percentage of innate cells. **(D)** Clustergram (Fernandez et al., 2017) of median expression of canonical markers used to identify individual clusters. **(E)** Density tSNE plots of each group. **(F and G)** Neutrophils (F) and monocytes (G) expressed as a percentage of circulating innate cells. Each dot represents one patient. Box plots represent mean ± SE. *, P < 0.05. cGA, corrected GA; dx, diagnosis; K-W, Kruskal-Wallis test.

we performed scRNA-seq of small intestinal tissue using the 10× Genomics Chromium platform (Luo et al., 2020). We analyzed six samples (fetal, *n* = 2; neonatal, *n* = 2; NEC, *n* = 2 [one sample excluded for low cell number]) matched to the suspension CyTOF cohort.

In total, we were able to sequence 30,269 cells ranging from 3,525 to 8,935 cells per sample and detecting a total of 23,329 genes with a mean expression of at least 1 unique molecular identifier per million reads across the dataset. Data were filtered based on the number of expressed genes (>200 and <7,000)

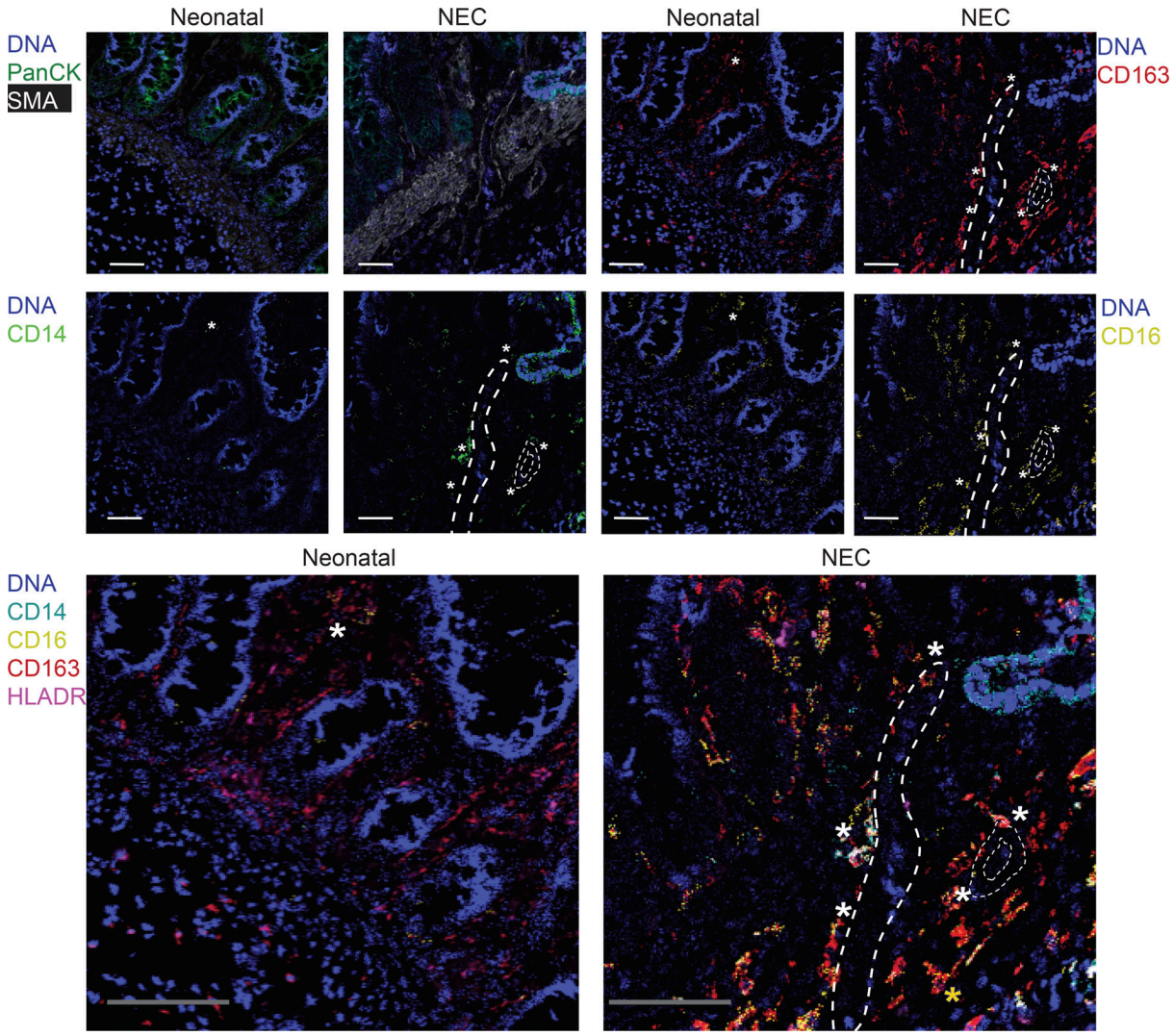

Figure 4. **IMC reveals that CD16⁺CD163⁺ monocytes are adjacent to blood vessels in NEC mucosa.** Composite of surface markers (individual layers) of interest generated from MCD files using histocat 1.7.6.1 (Fluidigm) from representative neonatal and NEC samples, White scale bar, 50 µm. Gray scale bar, 100 µm. White asterisk denotes one CD16⁺CD163⁺ monocyte. DNA, 191Ir DNA.

detected in each cell and containing <25% mitochondrial genes (Fig. S4 A) and were merged to perform a uniform manifold approximation and projection (UMAP) plot for dimension reduction and visualization of the clustering of individual cells (Fig. 6, A and B). The expression of the top 10 differentially expressed (DE) genes (Fig. S4 B) was used to annotate clusters into six broad groups: T cells, B cells, NK cells, Mϕ or DCs (MP/DC), and nonimmune cells (Fig. 6, A and B; and Fig. S4, B–D).

Based on expression of HLA-DR, CD14, CD16, and CD163 transcripts, we identified cluster 3 (Fig. 6, A–D) as the cluster containing the monocytes/Mϕ of interest identified in CyTOF analysis. Consistent with the CyTOF analysis, cluster 3 was enriched in NEC mucosa compared with fetal and neonatal intestine (Fig. 6 D and Fig. S4 C).

CD16⁺CD163⁺ monocytes/Mϕ are proinflammatory with high chemotaxis, ROS, and phagocytic activity

To further characterize CD16⁺CD163⁺ monocytes/Mϕ, we performed a post hoc cluster analysis of cluster 3. The resulting analysis yielded nine clusters that were present in two or more samples (Fig. 6, E and F). Clusters 1 and 2 (MC1 and MC2) had the highest expression of CD14, CD16, and CD163 and, as such, represented the clusters containing the monocytes/Mϕ of interest (Fig. 6 G and Fig. S4 E). Consistent with our CyTOF data, these two clusters were abundant in NEC (Fig. 6 H).

DE analysis revealed that cells in clusters MC1 and MC2 were transcriptionally distinct from other monocytes (MC0, MC3, MC4, MC5, MC6, MC7, and MC8; Fig. 7 A and Fig. S4 F). Interestingly, numerous inflammatory genes were enriched in the MC1 and MC2 monocytes and those associated with tissue repair and antigen presentation in the other monocyte clusters (Fig. 7, A–C). Specifically, expression of S100A8 and S100A9 (together known as calprotectin), IL-1B, IL-8 (CXCL8), and nuclear factor κ-light-chain enhancer of activated B cells 1A (NFKB1A) genes was increased in clusters MC1 and MC2 (Fig. 7, A–C). The Nanostring data had shown elevation of these same genes in bulk NEC tissue compared with neonatal controls (Fig. S1 D).

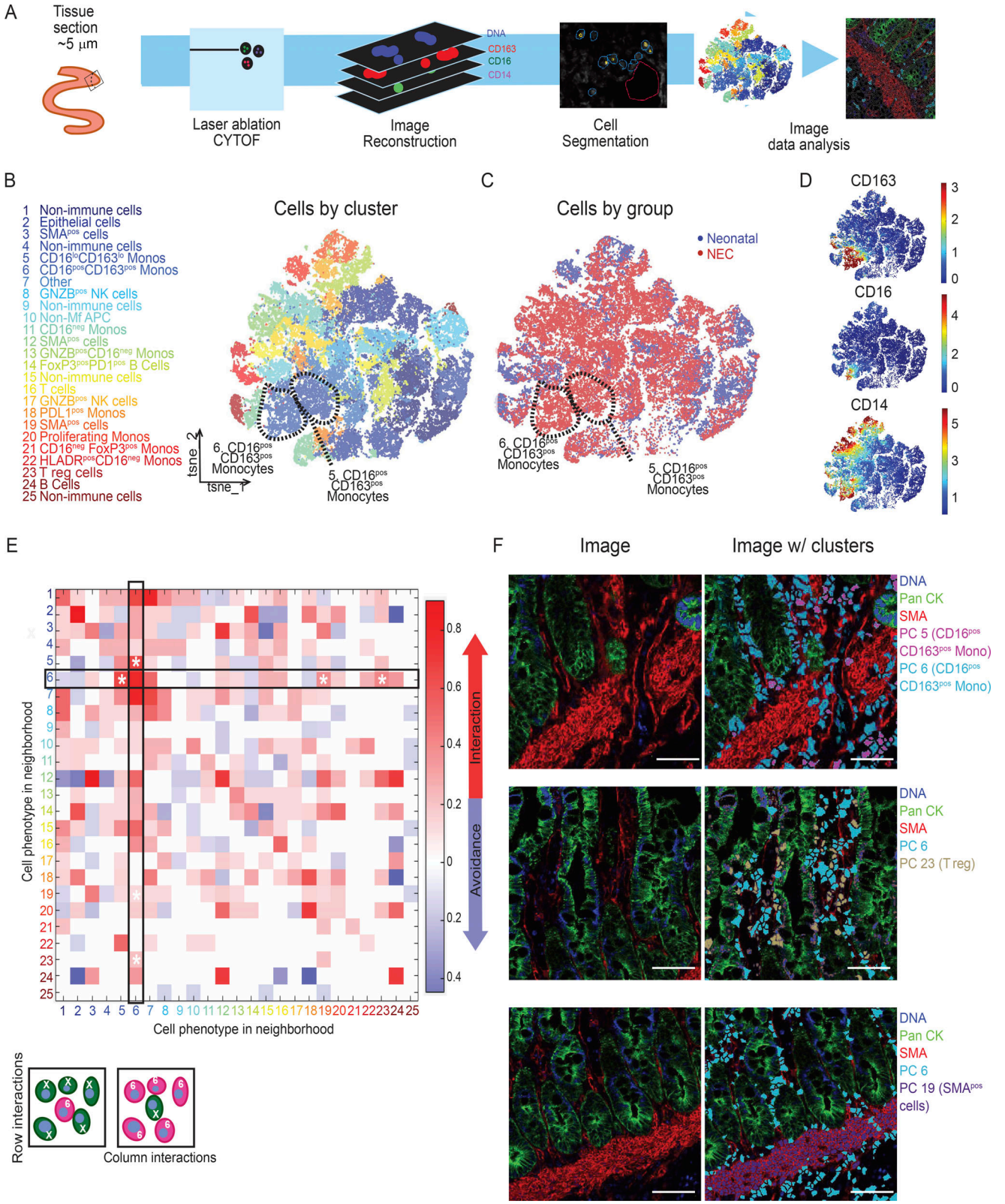

Figure 5. **IMC reveals numerous interactions of CD16⁺CD163⁺ monocytes/Mϕ in NEC-affected mucosa. (A–C)** IMC data collection and analysis pipeline adapted from Wang et al. (2019). Phenograph clustering using histocat 1.7.6.1 on CD45, CD3, CD19, CD14, CD16, CD163, and HLA-DR of cells from IMC of NEC (n = 6) and neonatal (n = 3) visualized by tSNE by clusters (B) and by group (C) with CD16⁺CD163⁺ monocytes/Mϕ denoted by black dashed lines. **(D)** Clusters of interest were identified using heatmaps in (Fig. S4 C). **(E)** Nearest neighbor analysis using histoCAT++ with cells that are <3 pixels apart and have a significant ($P < 0.01$) interaction (red) or avoidance (blue). Interesting interactions are highlighted with a white asterisk. **(F)** CD16⁺CD163⁺ monocytes/Mϕ (phenographs 5 and 6) are depicted in multiple layers (top, right). Phenograph 6 (CD16⁺CD163⁺ monocytes/Mϕ) are noted to be interacting with phenograph 19 (SMA⁺ cells) and phenograph 23 (T reg cells) in representative IMC images from one NEC sample (also shown in Fig. S3 A). Scale bar, 50 μM. MΦ, macrophage.

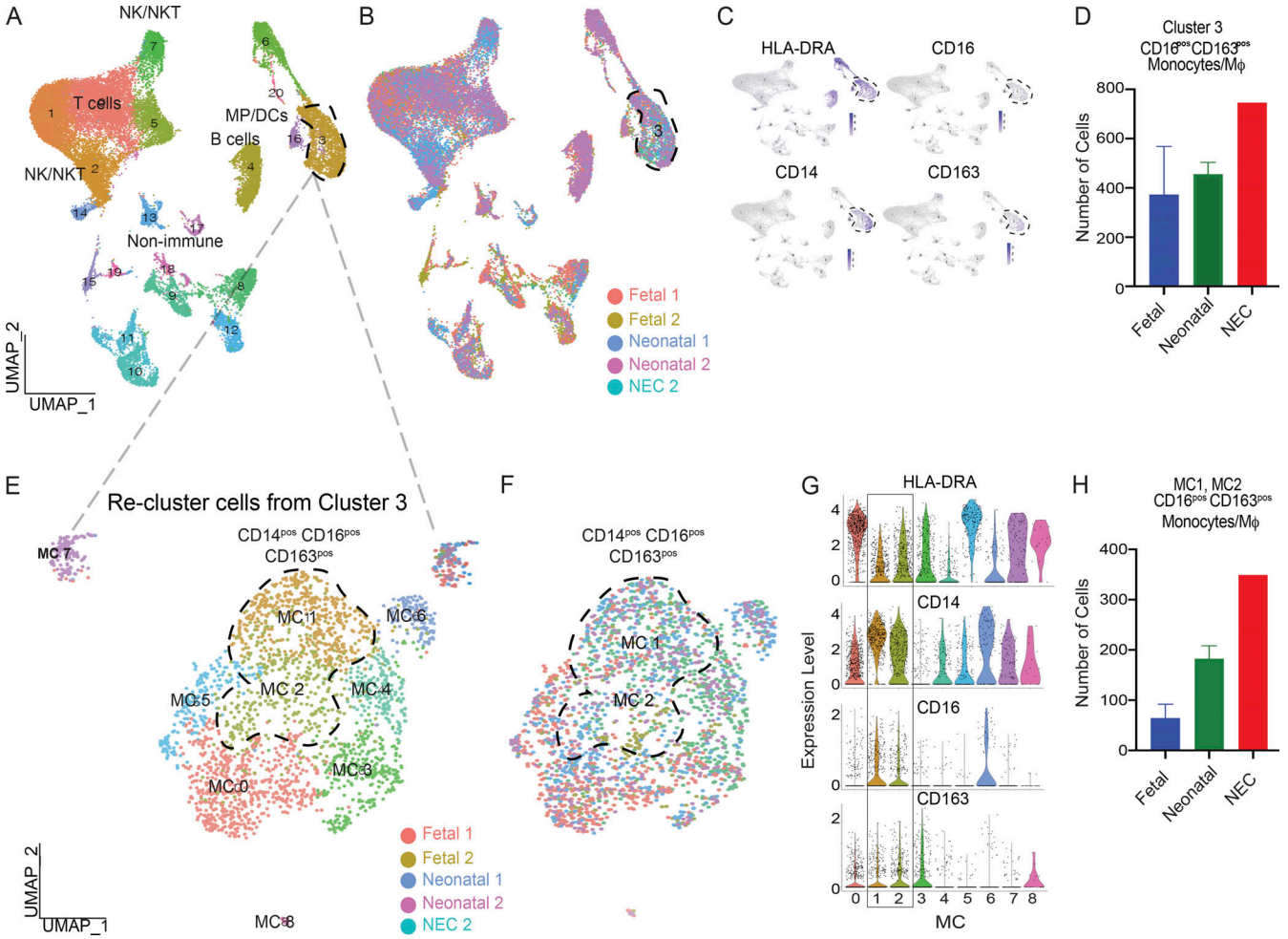

Figure 6. **scRNA-seq confirms that CD16⁺CD163⁺ monocytes/Mϕ are abundant in NEC mucosa. (A and B)** UMAP of all small intestinal cells colored by cluster (A) and by sample (B) of 30,269 cells from five biologically independent samples. **(C)** UMAP of expression level of genes used to identify monocytes of interest (cluster 3, dashed black lines), namely HLA-DR, CD14, CD16, and CD163. **(D)** Abundance of cells in cluster 3 in each group. **(E and F)** UMAP embedding showing rerun of cells from cluster 3 colored by cluster (E) and by sample (F; *n* = 2,402 monocytes from five biologically independent samples. **(G)** Violin plots of gene expression level within each cluster showing cells in MC1 and MC2, with highest expression of CD14, CD16, and CD163. **(H)** Cumulative data total number of cells in MC1 and MC2 within each group.

Taken together, these data suggest that the CD16⁺CD163⁺ monocytes/Mϕ secrete a large number of inflammatory factors and are the likely source of these genes in NEC tissue.

Additionally, we noted that several other genes involved in modulating inflammation in monocytes/Mϕ were differentially expressed in CD16⁺CD163⁺ monocytes/Mϕ. Triggering receptors expressed on myeloid cells 1 (TREM1), macrophage inflammatory protein 2α (CXCL2, a cytokine that participates in neutrophil recruitment), macrophage inflammatory protein 2β (CXCL3), as well as other genes in the IL-1 cytokine family (IL1A) were all significantly elevated in MC1 and MC2 monocytes compared with other monocytes. IL1R1, a gene that antagonizes IL-1 signaling, and HES1, a transcriptional repressor that attenuates inflammation (Shang et al., 2016), were downregulated, implying a highly inflammatory phenotype for CD16⁺CD163⁺ monocytes/Mϕ (Fig. 7, A–C).

Given that the CyTOF analysis demonstrated an increase in CD16⁺CD163⁺ monocytes/Mϕ both in the tissue and in the periphery (Figs. 2 E and 3 G) and that the IMC analysis identified them to be near blood vessels (Fig. 4), we hypothesized that these cells migrated from the periphery to inflamed tissue. In support of this hypothesis, the DE analysis identified that the expression of chemokines required for monocyte migration (CCL2, CCL7, CXCL5, and CXCL1) were significantly increased in cells in clusters MC1 and MC2 compared with other monocytes (Fig. 7, A and B). Consistent with this observation, gene set enrichment analysis (GSEA) revealed that pathways related to leukocyte transendothelial migration and chemotaxis were significantly enriched in MC1 and MC2 compared with other monocytes (Fig. 7 D and Fig. S4 F).

Further analysis of GSEA uncovered 188 pathways (Table S4) that were significantly altered ($q < 0.05$) in the MC1 and MC2 monocytes compared with other monocytes, including upregulation of TLR activation; ROS production; and cytokine signaling, including IL-17 signaling (Fig. 7 D and Fig. S4 F). Finally, Ingenuity Pathway Analysis (IPA) of the DE genes restricted to only the CD16⁺CD163⁺ monocytes/Mϕ from MC1 and MC2 with

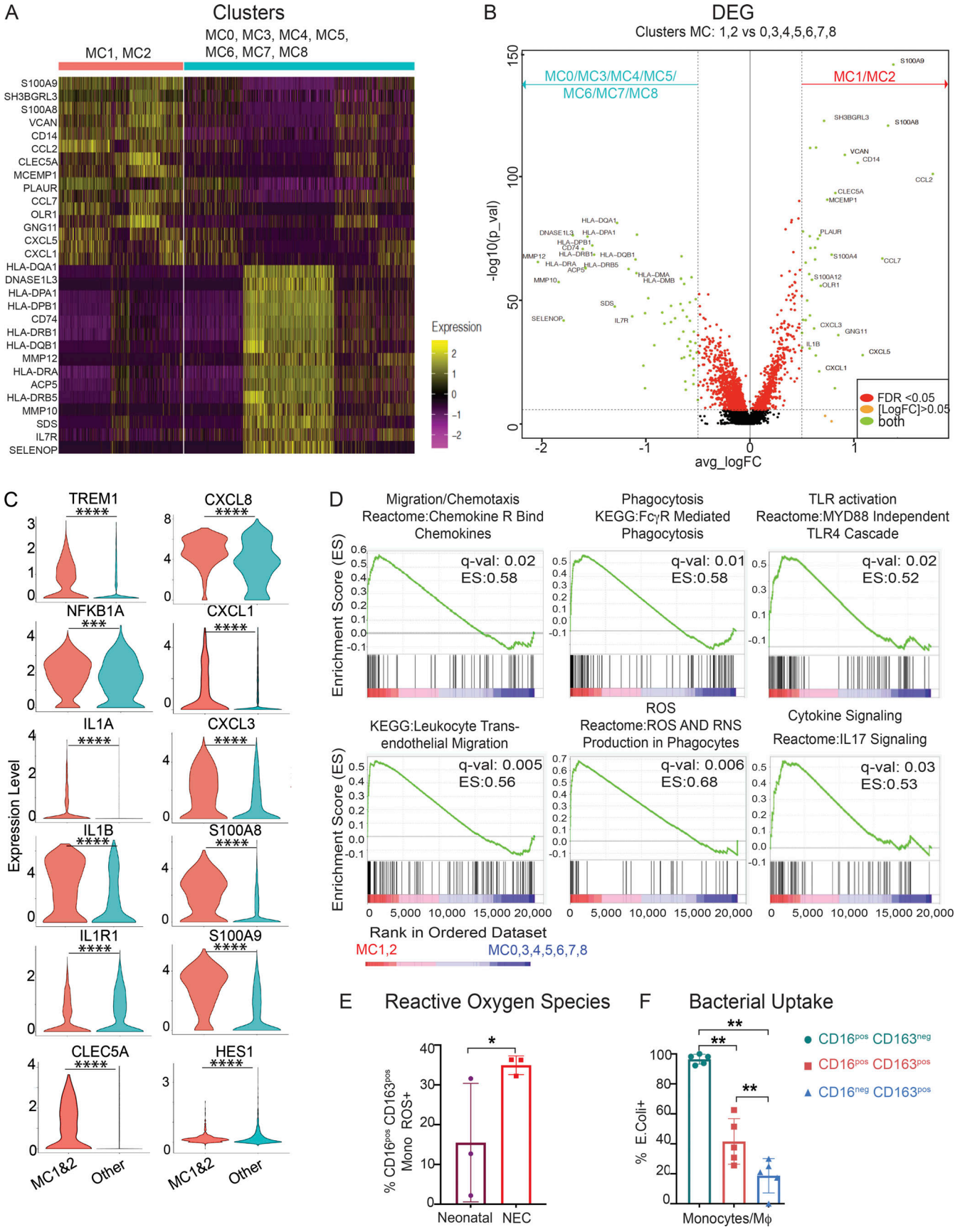
A
Clusters
MC1, MC2
MC0, MC3, MC4, MC5, MC6, MC7, MC8
S100A9
SH3BGRL3
S100A8
VCAN
CD14
CCL2
CLEC5A
MCEMP1
PLAUR
CCL7
OLR1
GNG11
CXCL5
CXCL1
HLA-DQA1
DNASE1L3
HLA-DPA1
HLA-DPB1
CD74
HLA-DRB1
HLA-DQB1
MMP12
HLA-DRA
ACP5
HLA-DRB5
MMP10
SDS
IL7R
SELENOP
Expression
B
DEG
Clusters MC: 1,2 vs 0,3,4,5,6,7,8
MC0/MC3/MC4/MC5/ MC6/MC7/MC8
MC1/MC2
-log10(p_val)
avg_logFC
FDR <0.05
[LogFC]>0.05
both
C
TREM1
CXCL8
NFKB1A
CXCL1
IL1A
CXCL3
IL1B
S100A8
IL1R1
S100A9
CLEC5A
HES1
Expression Level
MC1&2
Other
D
Migration/Chemotaxis
Reactome:Chemokine R Bind Chemokines
q-val: 0.02
ES:0.58
Phagocytosis
KEGG:FcγR Mediated Phagocytosis
q-val: 0.01
ES:0.58
TLR activation
Reactome:MYD88 Independent TLR4 Cascade
q-val: 0.02
ES:0.52
KEGG:Leukocyte Trans-endothelial Migration
q-val: 0.005
ES:0.56
ROS
Reactome:ROS AND RNS Production in Phagocytes
q-val: 0.006
ES:0.68
Cytokine Signaling
Reactome:IL17 Signaling
q-val: 0.03
ES:0.53
Enrichment Score (ES)
Rank in Ordered Dataset
MC1,2
MC0,3,4,5,6,7,8
E
Reactive Oxygen Species
% CD16pos CD163pos Mono ROS+
Neonatal
NEC
F
Bacterial Uptake
% E.Coli+
Monocytes/Mϕ
CD16pos CD163neg
CD16pos CD163pos
CD16neg CD163pos

Figure 7. **Inflammatory nature of CD16⁺CD163⁺ monocytes/Mϕ. (A)** Top 15 up- and downregulated genes in MC1 and MC2 compared with other monocytes (MC0, MC3, MC4, MC5, MC6, MC7, MC8). **(B)** Volcano plot of DE genes (DEG) with increased expression in MC1 and MC2 (red arrow on the right) and other monocytes (MC0, MC3, MC4, MC5, MC6, MC7, MC8; teal arrow on the left). **(C)** Violin plots of genes in inflammatory monocyte pathways with increased expression in MC1, MC2 (red) compared with other monocytes (teal). **(D)** Select GSEA pathways significantly enriched in MC1 and MC2 monocytes. **(E)** Box plot of ROS generation by CD16⁺CD163⁺ monocytes/Mϕ in NEC (n = 3) and neonatal (n = 3) tissue. **(F)** Box plot of *E. coli* (FITC) uptake by CD16⁺CD163⁻ monocytes/Mϕ, CD16⁺CD163⁺ monocytes/Mϕ, and CD16⁻CD163⁺ monocytes/Mϕ in small intestine samples (n = 5). *, P < 0.05; **, P < 0.01; ***, P < 0.001; ****, P < 0.0001. FC, fold change; FDR, false discovery rate; KEGG, Kyoto Encyclopedia of Genes and Genomes.

significant z-scores confirmed upregulation of similar pathways, including leukocyte extravasation, motility, chemokine, and TREM1 signaling (Fig. S4 G).

To confirm that CD16⁺CD163⁺ monocytes/Mϕ are potentially pathogenic in NEC and validate the scRNA-seq data, we examined ROS production and bacterial uptake in a subset of matched neonatal and NEC cases (Fig. S5, A–C; and Table S5) using flow cytometry. ROS production was increased in CD16⁺CD163⁺ monocytes/Mϕ in NEC mucosa compared with neonatal intestine (Fig. 7 E; and Fig. S5, A–C). We did not observe a difference in bacterial uptake by CD16⁺CD163⁺ monocytes/Mϕ in NEC versus neonatal intestinal tissue. However, CD16⁺CD163⁺ monocytes/Mϕ in all tissue examined had increased *Escherichia coli* uptake over CD163⁺ monocytes/Mϕ (Fig. 7 F; and Fig. S5, A–C)

Discussion

Current knowledge of peripheral and mucosal immune dysregulation in human NEC is limited to studies of specific immune subtypes and signaling pathways (Weitkamp et al., 2014; Hui et al., 2017; Egan et al., 2015). We have conducted deep phenotyping and transcriptional analysis of intestinal tissue from patients with NEC at a single-cell-level resolution linked to special information. The granularity afforded by single-cell analysis at the whole-tissue level allowed us not only to confirm that acute inflammation in intestinal tissue of patients with sNEC is characterized by increased abundance of both neutrophils and monocytes (MohanKumar et al., 2016; Emami et al., 2012) but also to identify the phenotypes of the particular neutrophils and monocytes/Mϕ that are enriched in NEC. Furthermore, we note dysregulation of other immune populations, including DCs, ILCs, and NK cells. We were also able to complement intestinal data with CyTOF analysis of peripheral blood, which revealed neutropenia and expansion of certain circulatory monocytes, suggesting a translocation of neutrophils and monocytes to the site of inflammation.

We observed abnormalities in multiple innate immune populations, including DCs, NK cells, and ILCs. Intestinal APCs, and CD103⁺ DCs in particular, maintain homeostasis and tolerance, recruit T cells into the intestinal tissue, and prime the adaptive immune system via antigen processing and presentation to T cells (Mann and Li, 2014; Ruane and Lavelle, 2011). CD103⁺ DCs were notably decreased in NEC, suggesting a potential decrease of priming and recruitment of T cells in affected mucosa and potentially decreased tolerance to commensal bacteria. Similarly, ckit⁺ ILCs, likely ILC3s, were diminished in NEC. It is possible that the decrease in ILCs is physiological because lymphoid tissue inducer cells, a subtype of ILC3, are involved in secondary lymphoid organ generation and decline once they have been established (Vivier et al., 2018; Stras et al., 2019). However, ILC3s play a crucial role in intestinal homeostasis and prevention of bacterial dissemination through regulating epithelial proliferation, intestinal regeneration, and production of anti-inflammatory cytokines and antimicrobial peptides (Romera-Hernández et al., 2020) and have been shown to be reduced in Crohn's disease (Zeng et al., 2019).

Interestingly, we were able to differentiate sNEC into three distinct phenotypes based on the type of neutrophilic infiltrates observed in NEC mucosa. The first group, consisting of ∼40% of NEC cases (C10 NEC) was enriched for neutrophils with increased expression of CD11b and CD38 or "aged" neutrophils. CD11b expression has been shown to be upregulated on aged neutrophils and is required for their migration to the sites of inflammation (Uhl et al., 2016). Similarly, CD38 expression on neutrophils is required for migration to the sites of inflammation (Partida-Sánchez et al., 2001). The second group, comprising ∼40% of NEC patients (C24 NEC) contained neutrophils with enhanced expression of CD56 and CXCR3 or "newly" recruited neutrophils. Specifically, CD56 expression is increased on newly infiltrating neutrophils (Hartl et al., 2008), and similarly, CXCR3 is important in recruiting neutrophils to the intestine during colitis (Chami et al., 2014). Finally, the third group, comprising ∼20% of cases (C9 NEC) consisted of immature (cKIT⁺) neutrophils. The C9 neutrophils were also enriched in other samples, including SIP and postNEC cases, suggesting that they might be important in tissue remodeling and not participate in acute inflammation. These results demonstrate that there are distinct phenotypes of patients with NEC based on their subtypes of neutrophils that likely correlate with the progression of the intestinal inflammation (C24 group with initial inflammation and the C10 group later on in the progression). Unfortunately, secondary to the deidentified nature of how the majority of these samples were collected, we do not have clinical data on the severity and timing of surgery in relationship to the disease course in the majority of these patients. It would be interesting to validate the correlation of the distinct phenotypes with the disease course in future studies.

This study is the first to identify the phenotype of the monocyte/Mϕ population enriched in NEC tissue. We identified CD16⁺CD163⁺ monocytes/Mϕ to be specifically enriched in tissue and circulation of patients with sNEC compared with all other groups. CD16⁺ (FcγRIII, capable of binding the Fc portion of IgG) monocytes have been shown to be highly phagocytic and secrete inflammatory cytokines such as IL-8 and IL-1β (Al-Rashed et al., 2019). They are also capable of upregulating CD163 on their surface (Alvarado-Vazquez et al., 2017). However, CD163, a

haptoglobin–hemoglobin scavenger receptor, is usually associated with alternatively activated or anti-inflammatory Mϕ (Alvarado-Vazquez et al., 2017) and in combination with CD64 (FcγRI), present on resident intestinal mucosal and muscularis layer Mϕ (Bain and Schridde, 2018). Interestingly, CD16$^+$CD163$^+$ monocytes have been described in numerous infectious and autoimmune diseases, including inflammatory bowel disease (Chapuy et al., 2019; Franzè et al., 2013); however, their function and transcriptional program has not been evaluated. scRNA-seq analysis of CD16$^+$CD163$^+$ monocytes/Mϕ demonstrated that they have an inflammatory M1-like signature with increased NF-κB, TREM1 IL-1β, IL-1α, and S100A8 and S100A9 expression. Given that these factors have been shown by our group and others (Aydemir et al., 2012; MacQueen et al., 2016) to be elevated in the tissues of patients with NEC, it is likely that their primary sources are the CD16$^+$CD163$^+$ monocytes/Mϕ. Moreover, CD16$^+$CD163$^+$ monocytes produce high amounts of IL-8 and CXCL1 and CXCL3 (factors involved in neutrophil chemoattraction; Alvarado-Vazquez et al., 2017). Consistent with their role in neutrophil recruitment, CD16$^+$CD163$^+$ monocytes/Mϕ were most abundant in the C24 neutrophil NEC subgroup that had an abundance of newly infiltrating neutrophils. GSEA analysis suggested that CD16$^+$CD163$^+$ monocytes/Mϕ were enriched for genes associated with phagocytosis, ROS production, and cytokine signaling. Moreover, a number of endogenous and exogenous TLR activation pathways were upregulated in these monocytes, confirming previous data implicating TLR signaling in NEC pathogenesis (Egan et al., 2015; Afrazi et al., 2014).

Combination of CyTOF analysis of peripheral blood of patients with surgical NEC and IMC analysis suggested that CD16$^+$CD163$^+$ monocytes/Mϕ migrate from the periphery and infiltrate all layers of intestinal mucosa. scRNA-seq analysis also identified genes involved in leukocyte transendothelial migration and chemotaxis to be upregulated in these monocytes. Moreover, CD16$^+$CD163$^+$ monocytes/Mϕ interacted with many immune and nonimmune intestinal cellular populations, including T reg cells, interactions that were much more prominent in NEC than neonatal samples. A decrease in T reg cells has been associated with NEC (Pang et al., 2018a), and alterations in T reg cell function with upregulation in inflammatory cytokines has been shown in inflammatory bowel disease (Mitsialis et al., 2020). Here, we show that CD16$^+$CD163$^+$ monocytes/Mϕ interact with T reg cells, suggesting that T reg cells attempt to suppress these monocytes/Mϕ, or alternatively, the inflammatory factors produced by CD16$^+$CD163$^+$ monocytes/Mϕ are inhibiting T reg cell function. Conversely, IMC identified reduced cell-to-cell interactions of anti-inflammatory cell types with other cells in NEC samples, reinforcing the switch to an inflammatory milieu in NEC. Collectively, our data highlight the important role that CD16$^+$CD163$^+$ monocytes/Mϕ play in all aspects of progressive intestinal inflammation in NEC and suggest that these cells are likely one of the pathogenic drivers of inflammation associated with NEC (Fig. 8). A subtype of NEC has been associated with RBC transfusions, where patients develop NEC hours after the transfusion. Given the role of CD163 as a hemoglobin scavenger, it is intriguing to think that CD16$^+$CD163$^+$ monocytes/Mϕ are also associated with transfusion-related NEC and should be assessed in the future.

The main limitations of our study were the relatively small sample size and lack of properly GA and chronological age–matched control tissues. Ideal control intestinal tissue would be from healthy premature infants, but these infants do not require procedures that allow for tissue collection. However, we have included numerous control groups in this study, including neonates who had non–NEC-related surgeries, infants with spontaneous ileal perforation, samples obtained at the reanastomosis surgery months after the NEC diagnosis, and second trimester fetal tissue, to overcome this limitation. Additionally, we did not have relevant clinical information to correlate the NEC phenotypes identified to disease severity and patient outcomes. Nevertheless, this study provides a deep phenotypic and functional analysis of NEC tissue that will serve as the foundation for future studies.

In summary, we provide a comprehensive analysis of dysregulation of innate immunity in NEC. Our data show distinct phenotypes of NEC that are determined by the identity of the neutrophilic infiltrate and elucidate the role of CD16$^+$CD163$^+$ monocytes/Mϕ in NEC pathogenesis. The implications of this study include an improved understanding of the innate immune dysregulation in NEC and identification of novel biomarkers and therapeutic targets in NEC to be evaluated in future studies.

Materials and methods

Human experimental guidelines

Small intestine tissue samples were obtained while following a discarded tissue protocol with approval of the institutional review board (IRB) at the University of Pittsburgh (IRB# PRO17070226). Patient consent was not obtained for the collection of discarded small intestine samples. The collection of peripheral blood samples occurred after parental consent was obtained with approval from the University of Pittsburgh IRB (IRB# PRO18010491).

Samples collected from Boston Children's Hospital (Table S1 B) were discarded samples obtained without patient consent. The IRB at Boston Children's Hospital/Harvard University approved tissue collection.

Intestinal tissue acquisition and storage

Fresh small intestinal tissue from surgical resections in infants were obtained with IRB approval (IRB# PRO17070226; Table S1). Human fetal small intestine was obtained through the University of Pittsburgh Biospecimen Core after IRB approval (IRB# PRO18010491; Table S1). Tissue was cryopreserved, and single cells were isolated as previously described (Stras et al., 2019). Briefly, intestinal tissue samples were cut into subcentimeter pieces and cryopreserved in freezing media (10% DMSO in FBS) at −80°C for 24 h and then transferred into liquid nitrogen until batch analysis.

Whole-blood RBC lysis

100–250 µl of whole blood from NEC and control patients (Table S1) was collected at the University of Pittsburgh Medical Center after consent (IRB# 19050118). Whole blood was placed in a BD Microtainer MAP K2EDTA 1.0-mg tube and stored at 4°C. Within 8 h, serial RBC lysis was performed as follows: (1) 5 ml of red cell

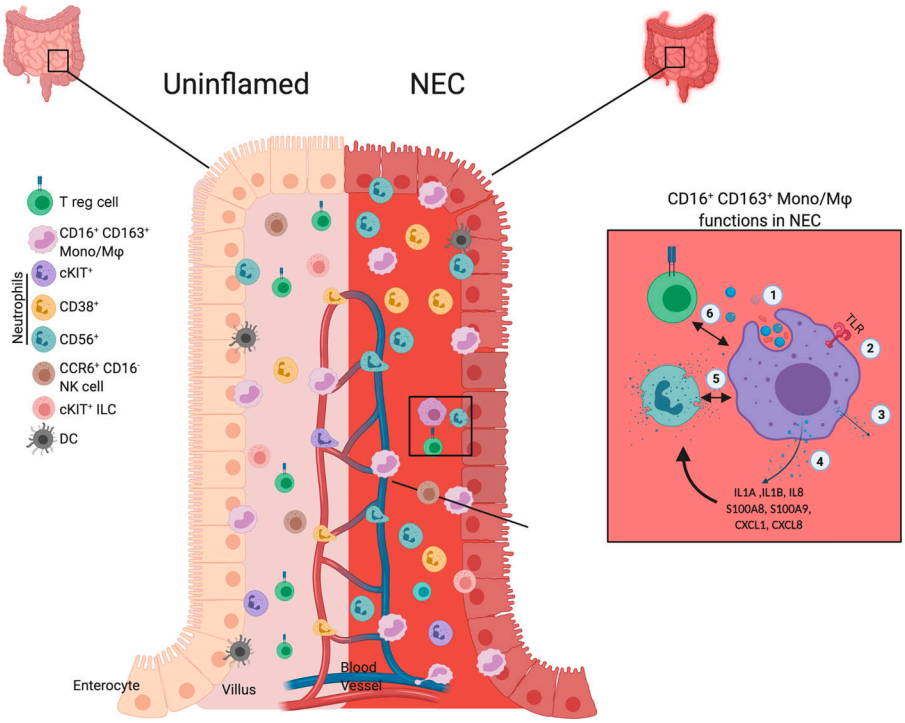

Figure 8. **Innate dysregulation in NEC.** Summary of the main findings of the study. The role of CD16⁺CD163⁺ monocytes/Mϕ in NEC includes: (1) phagocytosis, (2) increased TLR signaling, (3) increased ROS production, (4) increased secretion of inflammatory cytokines, (5) neutrophil recruitment, and (6) interaction with various cells including regulatory T cells.

lysis buffer (BioLegend) was added to 100 µl whole blood at room temperature for 15 min, (2) diluted to a total volume of 45 ml with Dulbecco's PBS (DPBS; Gibco), (3) centrifuged at 4°C at 1,500 rpm, and (4) decanted of supernatant. Steps 1–4 were repeated until there were no visible RBCs. Resulting cells were counted after suspension in DPBS. Cells were cryopreserved in freezing media similarly to intestinal tissue as outlined in Konnikova et al. (2018). At the time of analysis, samples were quickly thawed and washed in RPMI medium plus 10% FBS (Corning), 1× GlutaMax, 10 mM Hepes, 1× MEM nonessential amino acids, 1 mM sodium pyruvate, 100 IU/ml penicillin, and 100 µg/ml streptomycin.

Intestinal tissue digestion

Intestinal tissue samples were quickly thawed and washed in RPMI medium plus 10% FBS (Corning), 1× GlutaMax, 10 mM Hepes, 1× MEM nonessential amino acids, 1 mM sodium pyruvate, 100 IU/ml penicillin, and 100 µg/ml streptomycin. Next, intestinal tissue was incubated overnight in the same media with 1 µg/ml DNase 1 and 100 µg/ml collagenase A. Tissue dissociation was performed on the gentleMACS Octo Dissociator with heaters (Miltenyi Biotec) using the heated human tumor protocol 1. Tissue was then filtered through a 70-µm nylon mesh cell strainer (Sigma). A single-cell suspension was made by washing in DPBS without Ca^{2+} and Mg^{2+} (Sigma).

Suspension CyTOF staining/analysis

Circulating blood cells and intestinal tissue single cells (Table S1) were washed in cell-staining buffer (CSB), which consisted of DPBS with 0.5% BSA (Sigma) and 0.02% sodium azide incubated with Human TruStain FcX (BioLegend). Cells were stained with a cocktail of antibodies (Table S2) and washed in CSB, fixed in 1.6% paraformaldehyde (Sigma), and kept in CSB at 4°C overnight. The next day, samples were labeled with 191Ir/193Ir DNA intercalator (Fluidigm) and shipped overnight to the Longwood Medical Area CyTOF Core. MiliQ water was used to wash cells, and beads were added for normalization with subsequent analysis on a Helios mass cytometer (Fluidigm) in cell acquisition solution at a rate of 250 events/s. Data were bead normalized and exported as FCS files to the dfci pydio cloud.

Files were uploaded to the Premium Cytobank platform and gated on bead⁻, DNA⁺ for single cells and Rh103⁻ viable cells, initially. Manual gating was performed in Premium Cytobank for CD45⁺ immune cells and CD3⁻CD19⁻CD66b⁻ for innate cell analysis. CD45⁺ and CD3⁻CD19⁻CD66b⁻ cells were uploaded to Cytofkit (Chen et al., 2016a) as published (Stras et al., 2019) using R. Data were transformed with cytofAsinh, and FCS files were merged with ceil and dimensionality reduction with t-distributed stochastic neighbor embedding (tSNE). Phenograph clustering was performed using a preset k = 30. Cluster abundance was extracted and analyzed, and plots were generated using GraphPad Prism. In addition, mean metal intensity values for neutrophil clusters extracted for antibodies of interest were analyzed in GraphPad Prism 8.

IMC staining

Biopsy-sized pieces of small intestinal tissue were fixed in formalin on the day of collection and subsequently embedded in paraffin in batches. FFPE tissue was sectioned into 4–5-µm-thick sections. Slides were deparaffinized using xylene and alcohol and placed in 1× antigen retrieval buffer (#CTS013; R&D) at 95°C for 20 min. Next, slides were washed in distilled H_20 (ddH_20) and DDPBS (Gibco). Tissue was blocked with 3% BSA in DPBS for 45 min at room temperature. Overnight incubation of antibodies (Table S2) diluted in 0.5% BSA in DPBS at 4°C was performed. Slides were rinsed in DPBS with 0.1% Triton X-100 twice and

DPBS twice. Counterstain was performed with 191Ir/193Ir DNA intercalator (Fluidigm) at (1:2,000) in ddH_20 at room temperature for 30 min. Slides were rinsed in ddH_20 and then air dried.

Selection of areas of interest

Regions of small intestinal tissue were selected manually to capture all layers of the intestine. The same-sized area was scanned in all samples.

IMC image acquisition

The Helios CyTOF cytometer coupled to a Hyperion Imaging System (Fluidigm) was used to acquire data. An optical image of each slide was acquired using Hyperion software, and areas to ablate were selected as described above. Laser ablation was performed at a resolution of 4 µm and a frequency of 200 Hz. Data from slides were acquired over two consecutive days in a total of 11 image stacks from nine samples. One sample had a significantly smaller area of tissue and required three sections to be scanned to obtain the same total area.

IMC data segmentation and analysis

Data from Hyperion were extracted as MCD and TXT files, which were visualized using histoCAT++ (Fluidigm) to generate the images in Fig. 4. Further analysis of image data was performed using a recently published IMC segmentation pipeline (Damond et al., 2019) that was adapted to our dataset. Briefly, a Python script (https://github.com/BodenmillerGroup/imctools) was used to convert text format (TXT) files from data acquisition to TIFF images. Spillover compensation was performed to minimize crosstalk between channels. The images where segmented in two steps. First ilastik (Berg et al., 2019), an interactive machine learning software program, was used to classify pixels as nucleus, cytoplasm, or background components. Training of the Random Forest Classifier was performed on 125 × 125-pixel substacks generated from original images using relevant markers (e.g., CD45, CD3, CD14, CD163, panCK, SMA). Next, these probability maps were imported into CellProfiler to identify nuclei, define cell borders, and generate cell masks. Single cells were identified using these cell masks. This enabled extraction of single-cell information from original images. Files and masks were loaded to histoCAT 1.7.6.1 (Schapiro et al., 2017), visualized, and analyzed as follows. Phenograph clustering of cells was performed using major lineage markers to identify monocytes of interest. Clusters were visualized using the tSNE function and plots generated. Nearest neighborhood analysis was performed in histocat 1.7.6.1, identifying neighboring cells within 3 pixels to identify with interactions present in >10% of images with a of P value of 0.01. IMC raw counts were extracted for each cluster, and data were graphed using GraphPad Prism 8.

scRNA-seq: 10X

Cryopreserved intestinal samples were thawed and single-cell suspensions made as outlined above and per a previously published protocol (Konnikova et al., 2018). We selected for live cells using a live/dead kit. We used 3′ GEM libraries using the 10X kit from MedGenome. Sequencing was performed on HigSeq lanes with two samples per lane and with a target of 5,000 cells (Xin et al., 2020; Luo et al., 2020).

scRNA-seq: Data analysis

The scRNA-seq data were processed using the Cell Ranger 4.0.0 pipeline to align reads and generate a count matrix. Next, the output was analyzed with the R package Seurat 4.0. Cells with mitochondria reads >25% or samples where the number of genes was <200 or >7,000 were filtered out. The data were normalized using the "LogNormalize" method. This method normalizes the expression for each cell by the total expression, multiplies by a factor of 10,000, and log-transforms the data. The cells from different samples were integrated to minimize the batch effect. Next, the integrated expression for each gene was scaled to a mean and variance of 0 and 1, respectively, across cells. Graph-based clustering was implemented in Seurat, and the resulting clusters were visualized with UMAP, which identified 21 clusters. Clusters were identified based on canonical gene expression (Fig. S4). We further reclustered monocytes of interest ($CD16^+$, $CD163^+$, $HLA\text{-}DR^+$) in cluster 3 to identify nine distinct clusters. Among these nine clusters, clusters 1 and 2 were enriched in CD16, CD163, and HLA-DR. A DE analysis was performed to compare clusters 1 and 2 and the other clusters. The resulting $\log_{10}$ P values were plotted against $\log_2$ fold change in a volcano plot. We further performed GSEA using IPA. UMAP plots, gene expression plots, and violin plots were generated using R Seurat 4.0. Box plots of cluster abundance were generated using GraphPad Prism 8.

Flow cytometry staining

Single cells from intestinal tissue digestion were obtained as outlined above. Cells for the ROS experiment were stained with H2DCFDA (D399; Invitrogen) dissolved in DMSO at 37°C for 45 min. Samples were washed using FACS buffer at 3,000 rpm for 5 min. Cells were then stained with propidium iodide (PI) dye for 15 min at room temperature. Samples were then stained with antibody cocktail for 30 min on ice and washed with FACS buffer and fixed with paraformaldehyde. Samples were resuspended in FACS buffer.

Cells for the bacterial uptake experiment were added to serum-free DMEM (Gibco) with FITC-labeled *E. coli* and centrifuged at 1,500 rpm for 3–4 min and incubated at 37°C for 20 min. Cells were washed with PBS and then incubated with PI for 15 min at room temperature. Samples were washed in FACS buffer and stained with antibody cocktail for 30 min on ice. Cells were washed in FACS buffer again and then briefly incubated with trypan blue and fixed with paraformaldehyde. Cells from ROS and bacterial uptake were resuspended in FACS buffer.

Flow cytometry analysis

Flow cytometry was performed on an LSR II Analyzer (BD Biosciences) at the Yale University Flow Cytometry Core. Data were analyzed with FlowJo software.

mRNA extraction and IPA

Intestinal tissue from the Harvard University cohort (Table S1 B) were homogenized in Buffer RLT (QIAGEN) and processed using the nCounter Prep Station and Digital Analyzer according to the manufacturer's instructions (nCounter system; https://www.nanostring.com). A panel of 5 housekeeping genes and 79 genes

of interest was used to analyze the samples using previously published microarray data (Blanchard et al., 2006; Table S3). Data from neonatal controls served as the mean, and gene expression was expressed as z-scores for NEC and postNEC.

Statistical analysis

Kruskal-Wallis analysis and Dunn's multiple comparison test for post hoc analysis among groups were performed using R 3.6.1 software. One-tailed *t* test was used to compare two groups. Comparisons of mean expression values were corrected using the Bonferroni method. $P \leq 0.05$ was significant.

Plot generation

All graphs and heatmaps comparing multiple groups were generated using GraphPad Prism 8.

Online supplemental material

Fig. S1 summarizes additional data from suspension mass cytometry (CyTOF) and Nanostring experiments of small intestine. Fig. S2 summarizes additional data from peripheral blood CyTOF experiments. Fig. S3 summarizes additional data from the IMC analysis of small intestine. Fig. S4 summarizes additional data from scRNA-seq experiments. Fig. S5 contains the gating strategy for the flow cytometry experiments for ROS and bacterial uptake analysis. Table S1 contains demographic data for cases of small intestine and peripheral blood samples from all experiments. Table S2 lists antibodies used in CyTOF, IMC, and flow experiments. Table S3 lists the Nanostring genes. Table S4 lists the pathways from GSEA. Table S5 lists flow cytometry antibodies used in ROS and bacterial uptake experiments.

Data availability

Data analyzed in this study have been stored according to IRB guidelines and are subject to institutional regulations. Requests can be directed to the lead contact Liza Konnikova. Single-cell data related to all cells were deposited at Gene Expression Omnibus under accession number GSE178088.

Acknowledgments

We would like to thank all our patients and their families for their contribution to improving our understanding of NEC. Additionally, we are grateful to Dean Yimlamai and his group for help with sample collection and the Yale CyTOF core for helping with the IMC images.

This research was funded by the University of Pittsburgh, Yale School of Medicine, and Eunice Kennedy Shriver National Institute of Child Health and Human Development grant no. 1R21HD102565-01A1.

Author contributions: L. Konnikova conceived and supervised the work. O.O. Olaloye, J.M. Toothaker, C.C. McCourt, and J. Xiao processed tissue and performed suspension CyTOF and IMC. O.O. Olaloye analyzed all suspension and imaging CyTOF data. L.Werner and D. Shouval helped with data analysis. C.C. McCourt performed digestion and sample preparation for scRNA-seq. X. An and F. Wang performed library preparation for scRNA-seq supervised by K. Chen. P. Liu analyzed all scRNA-seq data with supervision by G. Tseng and L. Konnikova. B.T. McCourt and J.M. Toothaker performed ROS and phagocytosis flow experiments and analysis. J.D. Goldsmith and S.B. Snapper provided the Boston Children's Hospital cohort. J. Gringauz performed mRNA extraction for Nanostring, and E. Prochaska led the subsequent analysis. M. Good, O.O. Olaloye, L. Konnikova, S. Shaffer, UPMC NICU Faculty, and UPMC Pediatric Surgery Faculty were involved in patient identification, enrollment, and sample collection. O.O. Olaloye and L. Konnikova wrote the manuscript, and all authors contributed to the final draft.

Disclosures: M. Good reported grants from National Institutes of Health, Takeda Pharmaceuticals, and Astarte Medical Partners, and personal fees from Abbott Laboratories outside the submitted work; in addition, M. Good had a patent to use interleukin-22 for the prevention or treatment of necrotizing enterocolitis pending (PCT/US2017/027806). S.B. Snapper reported grants from Pfizer, Amgen, Novartis, and Takeda, personal fees from Pfizer, Amgen, Lilly, BMS, Pandion, Merck, and Takeda, and other from Pandion outside the submitted work. No other disclosures were reported.

Submitted: 26 February 2020
Revised: 8 February 2021
Accepted: 7 June 2021

References

Afrazi, A., M.F. Branca, C.P. Sodhi, M. Good, Y. Yamaguchi, C.E. Egan, P. Lu, H. Jia, S. Shaffiey, J. Lin, et al. 2014. Toll-like receptor 4-mediated endoplasmic reticulum stress in intestinal crypts induces necrotizing enterocolitis. *J. Biol. Chem.* 289:9584–9599. https://doi.org/10.1074/jbc.M113.526517

Al-Rashed, F., Z. Ahmad, M.A. Iskandar, J. Tuomilehto, F. Al-Mulla, and R. Ahmad. 2019. TNF-α induces a pro-inflammatory phenotypic shift in monocytes through ACSL1: relevance to metabolic inflammation. *Cell. Physiol. Biochem.* 52:397–407. https://doi.org/10.33594/000000028

Alvarado-Vazquez, P.A., L. Bernal, C.A. Paige, R.L. Grosick, C. Moracho Vilrriales, D.W. Ferreira, C. Ulecia-Morón, and E.A. Romero-Sandoval. 2017. Macrophage-specific nanotechnology-driven CD163 overexpression in human macrophages results in an M2 phenotype under inflammatory conditions. *Immunobiology*. 222:900–912. https://doi.org/10.1016/j.imbio.2017.05.011

Aydemir, G., F. Cekmez, I.A. Tanju, F.E. Canpolat, F.A. Genc, S. Yildirim, T. Tunc, and S.U. Sarici. 2012. Increased fecal calprotectin in preterm infants with necrotizing enterocolitis. *Clin. Lab.* 58:841–844.

Bain, C.C., and A. Schridde. 2018. Origin, differentiation, and function of intestinal macrophages. *Front. Immunol.* 9:2733. https://doi.org/10.3389/fimmu.2018.02733

Berg, S., D. Kutra, T. Kroeger, C.N. Straehle, B.X. Kausler, C. Haubold, M. Schiegg, J. Ales, T. Beier, M. Rudy, et al. 2019. ilastik: interactive machine learning for (bio)image analysis. *Nat. Methods.* 16:1226–1232. https://doi.org/10.1038/s41592-019-0582-9

Bhatia, A.M., B.J. Stoll, M.J. Cismowski, and S.E. Hamrick. 2014. Cytokine levels in the preterm infant with neonatal intestinal injury. *Am. J. Perinatol.* 31:489–496.

Blanchard, C., N. Wang, K.F. Stringer, A. Mishra, P.C. Fulkerson, J.P. Abonia, S.C. Jameson, C. Kirby, M.R. Konikoff, M.H. Collins, et al. 2006. Eotaxin-3 and a uniquely conserved gene-expression profile in eosinophilic esophagitis. *J. Clin. Invest.* 116:536–547. https://doi.org/10.1172/JCI26679

Chami, B., A.W.S. Yeung, C. van Vreden, N.J.C. King, and S. Bao. 2014. The role of CXCR3 in DSS-induced colitis. *PLoS One.* 9:e101622. https://doi.org/10.1371/journal.pone.0101622

Chapuy, L., M. Bsat, S. Sarkizova, M. Rubio, A. Therrien, E. Wassef, M. Bouin, K. Orlicka, A. Weber, N. Hacohen, et al. 2019. Two distinct colonic CD14$^+$

subsets characterized by single-cell RNA profiling in Crohn's disease. *Mucosal Immunol.* 12:703–719. https://doi.org/10.1038/s41385-018-0126-0

Chen, H., M.C. Lau, M.T. Wong, E.W. Newell, M. Poidinger, and J. Chen. 2016a. Cytofkit: a bioconductor package for an integrated mass cytometry data analysis pipeline. *PLOS Comput. Biol.* 12:e1005112. https://doi.org/10.1371/journal.pcbi.1005112

Chen, Y., K.T. Chang, D.W. Lian, H. Lu, S. Roy, N.K. Laksmi, Y. Low, G. Krishnaswamy, A. Pierro, and C.C. Ong. 2016b. The role of ischemia in necrotizing enterocolitis. *J. Pediatr. Surg.* 51:1255–1261. https://doi.org/10.1016/j.jpedsurg.2015.12.015

Damond, N., S. Engler, V.R.T. Zanotelli, D. Schapiro, C.H. Wasserfall, I. Kusmartseva, H.S. Nick, F. Thorel, P.L. Herrera, M.A. Atkinson, and B. Bodenmiller. 2019. A map of human type 1 diabetes progression by imaging mass cytometry. *Cell Metab.* 29:755–768.e5. https://doi.org/10.1016/j.cmet.2018.11.014

Denning, T.L., A.M. Bhatia, A.F. Kane, R.M. Patel, and P.W. Denning. 2017. Pathogenesis of NEC: Role of the innate and adaptive immune response. *Semin. Perinatol.* 41:15–28. https://doi.org/10.1053/j.semperi.2016.09.014

Egan, C.E., C.P. Sodhi, M. Good, J. Lin, H. Jia, Y. Yamaguchi, P. Lu, C. Ma, M.F. Branca, S. Weyandt, et al. 2015. Toll-like receptor 4-mediated lymphocyte influx induces neonatal necrotizing enterocolitis. *J. Clin. Invest.* 126:495–508. https://doi.org/10.1172/JCI83356

Ellsbury, D.L., R.H. Clark, R. Ursprung, D.L. Handler, E.D. Dodd, and A.R. Spitzer. 2016. A multifaceted approach to improving outcomes in the NICU: the Pediatrix 100 000 Babies Campaign. *Pediatrics.* 137: e20150389. https://doi.org/10.1542/peds.2015-0389

Emami, C.N., R. Mittal, L. Wang, H.R. Ford, and N.V. Prasadarao. 2012. Role of neutrophils and macrophages in the pathogenesis of necrotizing enterocolitis caused by Cronobacter sakazakii. *J. Surg. Res.* 172:18–28. https://doi.org/10.1016/j.jss.2011.04.019

Fernandez, N.F., G.W. Gundersen, A. Rahman, M.L. Grimes, K. Rikova, P. Hornbeck, and A. Ma'ayan. 2017. Clustergrammer, a web-based heatmap visualization and analysis tool for high-dimensional biological data. *Sci. Data.* 4:170151. https://doi.org/10.1038/sdata.2017.151

Fites, J.S., M. Gui, J.F. Kernien, P. Negoro, Z. Dagher, D.B. Sykes, J.E. Nett, M.K. Mansour, and B.S. Klein. 2018. An unappreciated role for neutrophil-DC hybrids in immunity to invasive fungal infections. *PLoS Pathog.* 14:e1007073. https://doi.org/10.1371/journal.ppat.1007073

Franzè, E., R. Caruso, C. Stolfi, M. Sarra, M.L. Cupi, F. Caprioli, I. Monteleone, F. Zorzi, D. De Nitto, A. Colantoni, et al. 2013. Lesional accumulation of CD163-expressing cells in the gut of patients with inflammatory bowel disease. *PLoS One.* 8:e69839. https://doi.org/10.1371/journal.pone.0069839

Guillet, R., B.J. Stoll, C.M. Cotten, M. Gantz, S. McDonald, W.K. Poole, and D.L. Phelps. National Institute of Child Health and Human Development Neonatal Research Network. 2006. Association of H2-blocker therapy and higher incidence of necrotizing enterocolitis in very low birth weight infants. *Pediatrics.* 117:e137–e142. https://doi.org/10.1542/peds.2005-1543

Hartl, D., S. Krauss-Etschmann, B. Koller, P.L. Hordijk, T.W. Kuijpers, F. Hoffmann, A. Hector, E. Eber, V. Marcos, I. Bittmann, et al. 2008. Infiltrated neutrophils acquire novel chemokine receptor expression and chemokine responsiveness in chronic inflammatory lung diseases. *J. Immunol.* 181: 8053–8067. https://doi.org/10.4049/jimmunol.181.11.8053

Hobbs, J.R., and J.A. Davis. 1967. Serum gamma-G-globulin levels and gestational age in premature babies. *Lancet.* 289:757–759. https://doi.org/10.1016/S0140-6736(67)91369-4

Holman, R.C., B.J. Stoll, A.T. Curns, K.L. Yorita, C.A. Steiner, and L.B. Schonberger. 2006. Necrotising enterocolitis hospitalisations among neonates in the United States. *Paediatr. Perinat. Epidemiol.* 20:498–506. https://doi.org/10.1111/j.1365-3016.2006.00756.x

Houben, C.H., X.N. Feng, K.W.E. Chan, J.W.C. Mou, Y.H. Tam, and K.H. Lee. 2017. Spontaneous intestinal perforation: the long-term outcome. *Eur. J. Pediatr. Surg.* 27:346–351. https://doi.org/10.1055/s-0036-1593990

Hristodorov, D., R. Mladenov, V. von Felbert, M. Huhn, R. Fischer, S. Barth, and T. Thepen. 2015. Targeting CD64 mediates elimination of M1 but not M2 macrophages in vitro and in cutaneous inflammation in mice and patient biopsies. *MAbs.* 7:853–862. https://doi.org/10.1080/19420862.2015.1066950

Hui, L., Y. Dai, Z. Guo, J. Zhang, F. Zheng, X. Bian, Z. Wu, Q. Jiang, M. Guo, K. Ma, and J. Zhang. 2017. Immunoregulation effects of different γδT cells and toll-like receptor signaling pathways in neonatal necrotizing enterocolitis. *Medicine (Baltimore).* 96:e6077. https://doi.org/10.1097/MD.0000000000006077

Hutter, J.J. Jr., W.E. Hathaway, and E.R. Wayne. 1976. Hematologic abnormalities in severe neonatal necrotizing enterocolitis. *J. Pediatr.* 88: 1026–1031. https://doi.org/10.1016/S0022-3476(76)81069-4

Jennewein, M.F., B. Abu-Raya, Y. Jiang, G. Alter, and A. Marchant. 2017. Transfer of maternal immunity and programming of the newborn immune system. *Semin. Immunopathol.* 39:605–613. https://doi.org/10.1007/s00281-017-0653-x

Jones, I.H., and N.J. Hall. 2020. Contemporary outcomes for infants with necrotizing enterocolitis–a systematic review. *J. Pediatr.* 220:86–92.e3. https://doi.org/10.1016/j.jpeds.2019.11.011

Konnikova, L., G. Boschetti, A. Rahman, V. Mitsialis, J. Lord, C. Richmond, V.T. Tomov, W. Gordon, S. Jelinsky, J. Canavan, et al. 2018. High-dimensional immune phenotyping and transcriptional analyses reveal robust recovery of viable human immune and epithelial cells from frozen gastrointestinal tissue. *Mucosal Immunol.* 11:1684–1693. https://doi.org/10.1038/s41385-018-0047-y

Li, N., V. van Unen, T. Abdelaal, N. Guo, S.A. Kasatskaya, K. Ladell, J.E. McLaren, E.S. Egorov, M. Izraelson, S.M. Chuva de Sousa Lopes, et al. 2019. Memory $CD4^+$ T cells are generated in the human fetal intestine. *Nat. Immunol.* 20:301–312. https://doi.org/10.1038/s41590-018-0294-9

Liu, L., H.L. Johnson, S. Cousens, J. Perin, S. Scott, J.E. Lawn, I. Rudan, H. Campbell, R. Cibulskis, M. Li, et al. Child Health Epidemiology Reference Group of WHO and UNICEF. 2012. Global, regional, and national causes of child mortality: an updated systematic analysis for 2010 with time trends since 2000. *Lancet.* 379:2151–2161. https://doi.org/10.1016/S0140-6736(12)60560-1

Luo, J., C.A. Erb, and K. Chen. 2020. Simultaneous measurement of surface proteins and gene expression from single cells. *Methods Mol. Biol.* 2111: 35–46. https://doi.org/10.1007/978-1-0716-0266-9_3

MacQueen, B.C., R.D. Christensen, C.C. Yost, D.K. Lambert, V.L. Baer, M.J. Sheffield, P.V. Gordon, M.J. Cody, E. Gerday, R. Schlaberg, et al. 2016. Elevated fecal calprotectin levels during necrotizing enterocolitis are associated with activated neutrophils extruding neutrophil extracellular traps. *J. Perinatol.* 36:862–869. https://doi.org/10.1038/jp.2016.105

Managlia, E., S.X.L. Liu, X. Yan, X.D. Tan, P.M. Chou, T.A. Barrett, and I.G. De Plaen. 2019. Blocking NF-κB activation in $Ly6c^+$ monocytes attenuates necrotizing enterocolitis. *Am. J. Pathol.* 189:604–618. https://doi.org/10.1016/j.ajpath.2018.11.015

Mann, E.R., and X. Li. 2014. Intestinal antigen-presenting cells in mucosal immune homeostasis: crosstalk between dendritic cells, macrophages and B-cells. *World J. Gastroenterol.* 20:9653–9664. https://doi.org/10.3748/wjg.v20.i29.9653

Mitsialis, V., S. Wall, P. Liu, J. Ordovas-Montanes, T. Parmet, M. Vukovic, D. Spencer, M. Field, C. McCourt, J. Toothaker, et al. Brigham and Women's Hospital Crohn's and Colitis Center. 2020. Single-cell analyses of colon and blood reveal distinct immune cell signatures of ulcerative colitis and Crohn's disease. *Gastroenterology.* 159:591–608.e10. https://doi.org/10.1053/j.gastro.2020.04.074

MohanKumar, K., K. Namachivayam, K.C. Chapalamadugu, S.A. Garzon, M.H. Premkumar, S.M. Tipparaju, and A. Maheshwari. 2016. Smad7 interrupts TGF-β signaling in intestinal macrophages and promotes inflammatory activation of these cells during necrotizing enterocolitis. *Pediatr. Res.* 79:951–961. https://doi.org/10.1038/pr.2016.18

Narasimhan, P.B., P. Marcovecchio, A.A.J. Hamers, and C.C. Hedrick. 2019. Nonclassical monocytes in health and disease. *Annu. Rev. Immunol.* 37: 439–456. https://doi.org/10.1146/annurev-immunol-042617-053119

Neu, J., and W.A. Walker. 2011. Necrotizing enterocolitis. *N. Engl. J. Med.* 364: 255–264. https://doi.org/10.1056/NEJMra1005408

Neu, J., and M. Pammi. 2017. Pathogenesis of NEC: Impact of an altered intestinal microbiome. *Semin. Perinatol.* 41:29–35. https://doi.org/10.1053/j.semperi.2016.09.015

Pang, Y., X. Du, X. Xu, M. Wang, and Z. Li. 2018a. Impairment of regulatory T cells in patients with neonatal necrotizing enterocolitis. *Int. Immunopharmacol.* 63:19–25. https://doi.org/10.1016/j.intimp.2018.07.029

Pang, Y., X. Du, X. Xu, M. Wang, and Z. Li. 2018b. Monocyte activation and inflammation can exacerbate Treg/Th17 imbalance in infants with neonatal necrotizing enterocolitis. *Int. Immunopharmacol.* 59:354–360. https://doi.org/10.1016/j.intimp.2018.04.026

Partida-Sánchez, S., D.A. Cockayne, S. Monard, E.L. Jacobson, N. Oppenheimer, B. Garvy, K. Kusser, S. Goodrich, M. Howard, A. Harmsen, et al. 2001. Cyclic ADP-ribose production by CD38 regulates intracellular calcium release, extracellular calcium influx and chemotaxis in neutrophils and is required for bacterial clearance in vivo. *Nat. Med.* 7: 1209–1216. https://doi.org/10.1038/nm1101-1209

Patel, R.M., S. Kandefer, M.C. Walsh, E.F. Bell, W.A. Carlo, A.R. Laptook, P.J. Sánchez, S. Shankaran, K.P. Van Meurs, M.B. Ball, et al. Eunice Kennedy Shriver National Institute of Child Health and Human Development Neonatal Research Network. 2015. Causes and timing of death in extremely premature infants from 2000 through 2011. *N. Engl. J. Med.* 372:331–340. https://doi.org/10.1056/NEJMoa1403489

Pou, C., D. Nkulikiyimfura, E. Henckel, A. Olin, T. Lakshmikanth, J. Mikes, J. Wang, Y. Chen, A.K. Bernhardsson, A. Gustafsson, et al. 2019. The repertoire of maternal anti-viral antibodies in human newborns. *Nat. Med.* 25:591–596. https://doi.org/10.1038/s41591-019-0392-8

Purisch, S.E., and C. Gyamfi-Bannerman. 2017. Epidemiology of preterm birth. *Semin. Perinatol.* 41:387–391. https://doi.org/10.1053/j.semperi.2017.07.009

Romera-Hernández, M., P. Aparicio-Domingo, N. Papazian, J.J. Karrich, F. Cornelissen, R.M. Hoogenboezem, J.N. Samsom, and T. Cupedo. 2020. Yap1-driven intestinal repair is controlled by group 3 innate lymphoid cells. *Cell Rep.* 30:37–45.e3. https://doi.org/10.1016/j.celrep.2019.11.115

Ruane, D.T., and E.C. Lavelle. 2011. The role of $CD103^+$ dendritic cells in the intestinal mucosal immune system. *Front. Immunol.* 2:25. https://doi.org/10.3389/fimmu.2011.00025

Schapiro, D., H.W. Jackson, S. Raghuraman, J.R. Fischer, V.R.T. Zanotelli, D. Schulz, C. Giesen, R. Catena, Z. Varga, and B. Bodenmiller. 2017. histoCAT: analysis of cell phenotypes and interactions in multiplex image cytometry data. *Nat. Methods.* 14:873–876. https://doi.org/10.1038/nmeth.4391

Schreurs, R.R.C.E., M.E. Baumdick, A.F. Sagebiel, M. Kaufmann, M. Mokry, P.L. Klarenbeek, N. Schaltenberg, F.L. Steinert, J.M. van Rijn, A. Drewniak, et al. 2019. Human fetal TNF-α-cytokine-producing CD4+ effector memory t cells promote intestinal development and mediate inflammation early in life. *Immunity.* 50:462–476.e8. https://doi.org/10.1016/j.immuni.2018.12.010

Scott, C.L., A.M. Aumeunier, and A.M. Mowat. 2011. Intestinal CD103+ dendritic cells: master regulators of tolerance? *Trends Immunol.* 32:412–419. https://doi.org/10.1016/j.it.2011.06.003

Shang, Y., M. Coppo, T. He, F. Ning, L. Yu, L. Kang, B. Zhang, C. Ju, Y. Qiao, B. Zhao, et al. 2016. The transcriptional repressor Hes1 attenuates inflammation by regulating transcription elongation. *Nat. Immunol.* 17:930–937. https://doi.org/10.1038/ni.3486

Stras, S.F., L. Werner, J.M. Toothaker, O.O. Olaloye, A.L. Oldham, C.C. McCourt, Y.N. Lee, E. Rechavi, D.S. Shouval, and L. Konnikova. 2019. Maturation of the human intestinal immune system occurs early in fetal development. *Dev. Cell.* 51:357–373.e5. https://doi.org/10.1016/j.devcel.2019.09.008

Swindell, W.R., M.A. Beamer, M.K. Sarkar, S. Loftus, J. Fullmer, X. Xing, N.L. Ward, L.C. Tsoi, M.J. Kahlenberg, Y. Liang, and J.E. Gudjonsson. 2018. RNA-seq analysis of IL-1B and IL-36 responses in epidermal keratinocytes identifies a shared MyD88-dependent gene signature. *Front. Immunol.* 9:80. https://doi.org/10.3389/fimmu.2018.00080

Uhl, B., Y. Vadlau, G. Zuchtriegel, K. Nekolla, K. Sharaf, F. Gaertner, S. Massberg, F. Krombach, and C.A. Reichel. 2016. Aged neutrophils contribute to the first line of defense in the acute inflammatory response. *Blood.* 128:2327–2337. https://doi.org/10.1182/blood-2016-05-718999

Vivier, E., D. Artis, M. Colonna, A. Diefenbach, J.P. Di Santo, G. Eberl, S. Koyasu, R.M. Locksley, A.N.J. McKenzie, R.E. Mebius, et al. 2018. Innate lymphoid cells: 10 years on. *Cell.* 174:1054–1066. https://doi.org/10.1016/j.cell.2018.07.017

Wang, Y.J., D. Traum, J. Schug, L. Gao, C. Liu, M.A. Atkinson, A.C. Powers, M.D. Feldman, A. Naji, K.M. Chang, and K.H. Kaestner. HPAP Consortium. 2019. Multiplexed in situ imaging mass cytometry analysis of the human endocrine pancreas and immune system in type 1 diabetes. *Cell Metab.* 29:769–783.e4. https://doi.org/10.1016/j.cmet.2019.01.003

Weitkamp, J.-H., T. Koyama, M.T. Rock, H. Correa, J.A. Goettel, P. Matta, K. Oswald-Richter, M.J. Rosen, B.G. Engelhardt, D.J. Moore, and D.B. Polk. 2013. Necrotising enterocolitis is characterised by disrupted immune regulation and diminished mucosal regulatory (FOXP3)/effector (CD4, CD8) T cell ratios. *Gut.* 62:73–82. https://doi.org/10.1136/gutjnl-2011-301551

Weitkamp, J.-H., M.J. Rosen, Z. Zhao, T. Koyama, D. Geem, T.L. Denning, M.T. Rock, D.J. Moore, M.D. Halpern, P. Matta, and P.W. Denning. 2014. Small intestinal intraepithelial TCRγδ+ T lymphocytes are present in the premature intestine but selectively reduced in surgical necrotizing enterocolitis. *PLoS One.* 9:e99042. https://doi.org/10.1371/journal.pone.0099042

Wright, H.L., A.L. Cross, S.W. Edwards, and R.J. Moots. 2014. Effects of IL-6 and IL-6 blockade on neutrophil function in vitro and in vivo. *Rheumatology (Oxford).* 53:1321–1331. https://doi.org/10.1093/rheumatology/keu035

Xin, H., Q. Lian, Y. Jiang, J. Luo, X. Wang, C. Erb, Z. Xu, X. Zhang, E. Heidrich-O'Hare, Q. Yan, et al. 2020. GMM-Demux: sample demultiplexing, multiplet detection, experiment planning, and novel cell-type verification in single cell sequencing. *Genome Biol.* 21:188. https://doi.org/10.1186/s13059-020-02084-2

Xuan, W., Q. Qu, B. Zheng, S. Xiong, and G.H. Fan. 2015. The chemotaxis of M1 and M2 macrophages is regulated by different chemokines. *J. Leukoc. Biol.* 97:61–69. https://doi.org/10.1189/jlb.1A0314-170R

Yee, W.H., A.S. Soraisham, V.S. Shah, K. Aziz, W. Yoon, and S.K. Lee. Canadian Neonatal Network. 2012. Incidence and timing of presentation of necrotizing enterocolitis in preterm infants. *Pediatrics.* 129:e298–e304. https://doi.org/10.1542/peds.2011-2022

Zeng, B., S. Shi, G. Ashworth, C. Dong, J. Liu, and F. Xing. 2019. ILC3 function as a double-edged sword in inflammatory bowel diseases. *Cell Death Dis.* 10:315. https://doi.org/10.1038/s41419-019-1540-2

Supplemental material

Five tables are provided online as separate Word files. Table S1 contains demographic data for cases of small intestine and peripheral blood samples from all experiments. Table S2 lists antibodies used in CyTOF, IMC, and flow experiments. Table S3 lists the Nanostring genes. Table S4 lists the pathways from GSEA. Table S5 lists flow cytometry antibodies used in ROS and bacterial uptake experiments.

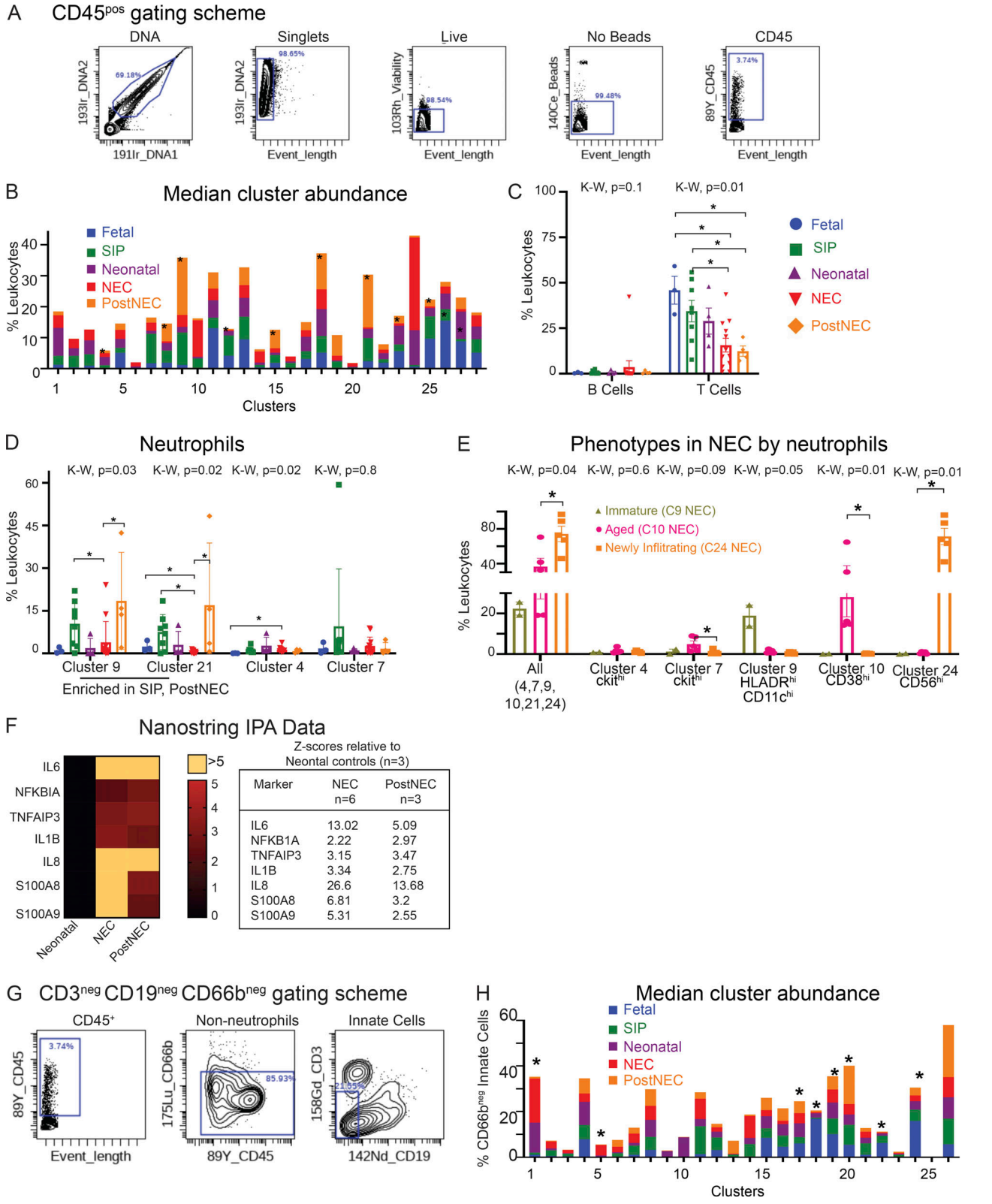

Figure S1. **Additional data from suspension mass cytometry (CyTOF) and Nanostring experiments of small intestine. (A)** Gating scheme to identify CD45⁺ cells exported for analysis from Premium Cytobank. **(B)** Abundance of each cluster in the various cohorts from CD45⁺ cell analysis. **(C–E)** B cells, T cells, neutrophil clusters, and neutrophil populations by NEC phenotype expressed as a percentage of leukocytes (immature [C9 NEC, *n* = 2], aged [C10 NEC, *n* = 5], and newly infiltrating [C24 NEC, *n* = 5]). **(F)** Relative z-scores of genes of interest from Nanostring IPA data in NEC and postNEC compared with neonatal cases. **(G)** Gating scheme to identify CD3⁻CD19⁻CD66b⁻ cells exported for analysis from Premium Cytobank. **(H)** Median cluster abundance for clusters from CD66b⁻ innate cell analysis. Asterisks denote clusters with significant differences between groups. Each dot represents one biological sample. Box plots represent mean ± SE. Fetal (*n* = 3), SIP (*n* = 8), neonatal (*n* = 4), NEC (*n* = 12), postNEC (*n* = 4). *, P < 0.05. K-W, Kruskal-Wallis test.

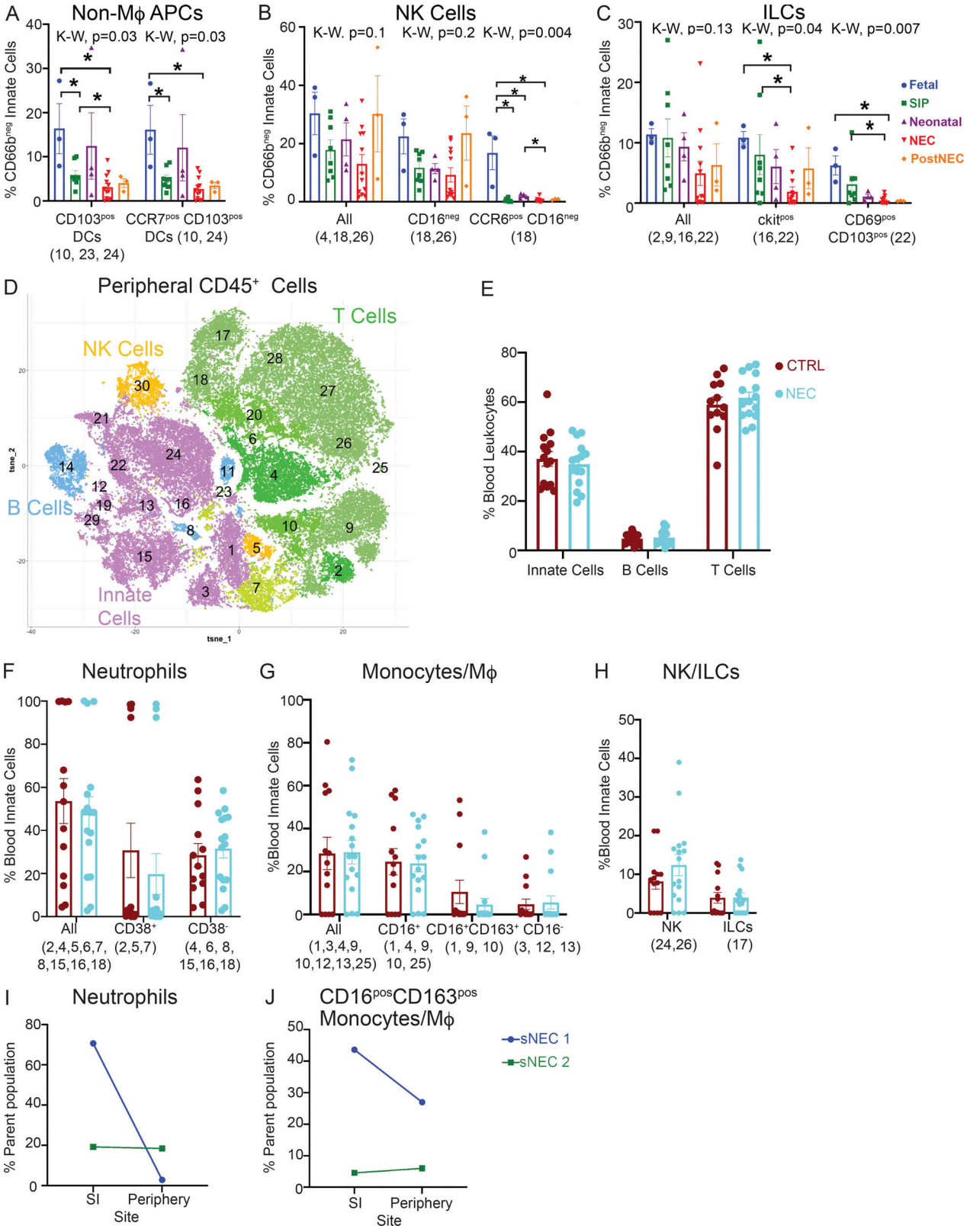

Figure S2. **Additional data from peripheral blood CyTOF experiments. (A–C)** Subtypes of nonmonocyte/Mϕ APCs (A), NK cells (B), and ILCs (C) expressed as a percentage of CD66b$^-$ innate cells. **(D)** tSNE of peripheral leukocytes. **(E)** Major populations expressed as a percentage of blood leukocytes. **(F–H)** Neutrophils (F), monocytes/Mϕ (G), and NK/ILCs (H) expressed as a percentage of innate cells in healthy control (CTRL) and all NEC samples. **(I and J)** Correlation between the abundance of neutrophils (I) and CD16$^+$CD163$^+$ monocytes/Mϕ (J) in small intestine (SI) and peripheral blood of matched sNEC cases. Each dot represents one patient sample. Box plots represent mean ± SE. CTRL (n = 13), mNEC (n = 12), and sNEC (n = 3). *, P < 0.05. K-W, Kruskal-Wallis test.

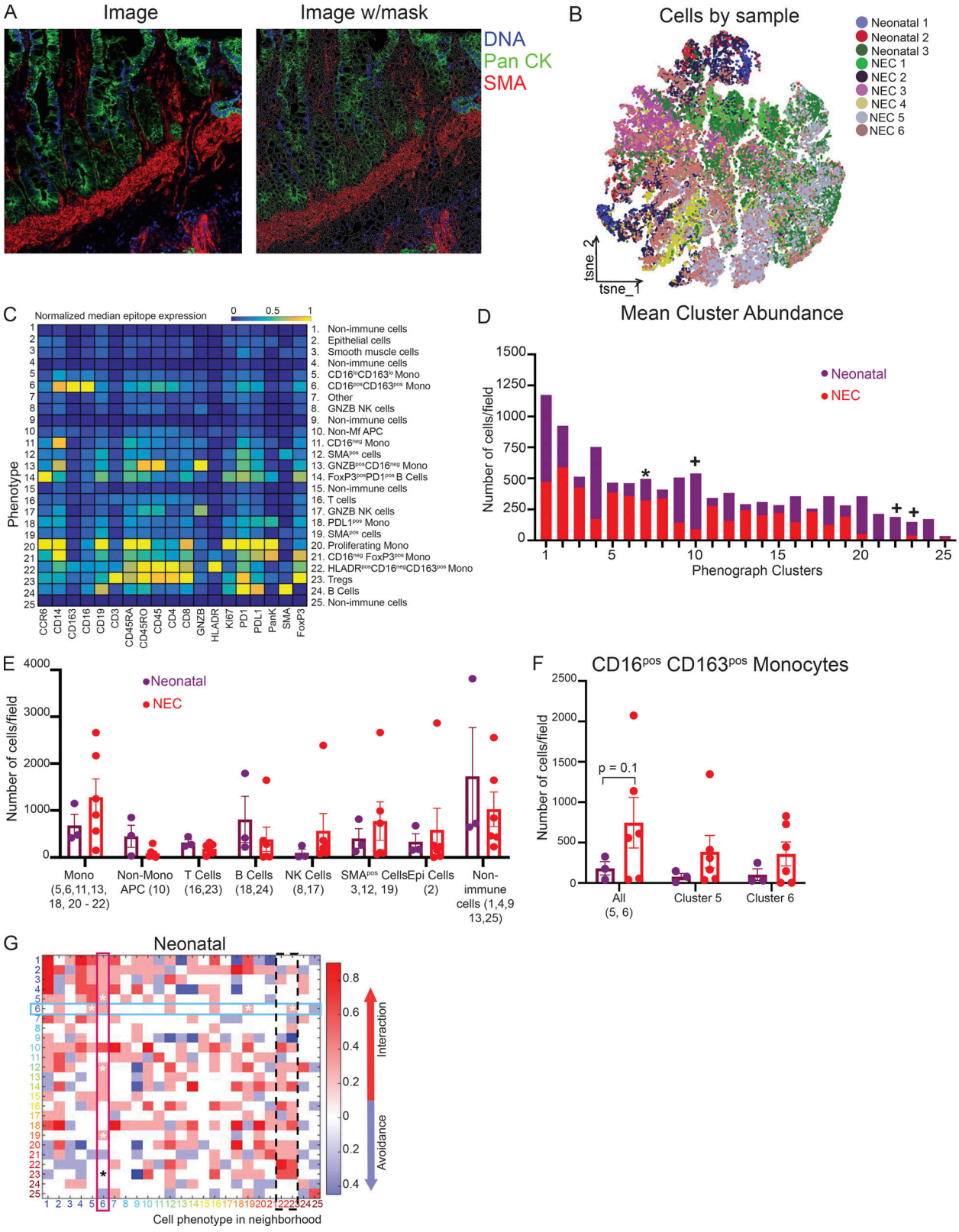

Figure S3. **Additional data from the analysis of IMC analysis of small intestine. (A)** Representative TIFF image (left) of one NEC sample (also in Fig. 5 F) generated from histoCAT 1.7.6 with individual cells highlighted in mask. **(B)** tSNE plot of phenograph clusters from Fig. 5, B and C, colored by individual samples. **(C)** Heatmap of canonical surface markers used to identify phenograph clusters in Fig. 5. **(D)** Median number of cells per field in each phenograph cluster in neonatal (n = 3) and NEC (n = 6) samples. **(E and F)** Number of cells per field in various populations (E) and in $CD16^{+}CD163^{+}$ monocytes (F). **(G)** Neighborhood analysis of cell-to-cell interactions in neonatal samples (n = 3). Each dot represents one sample. Box plots represent mean ± SE. *, P < 0.05; +, P < 0.1 by t test. CellsEpi, epithelial cells; MΦ, macrophage.

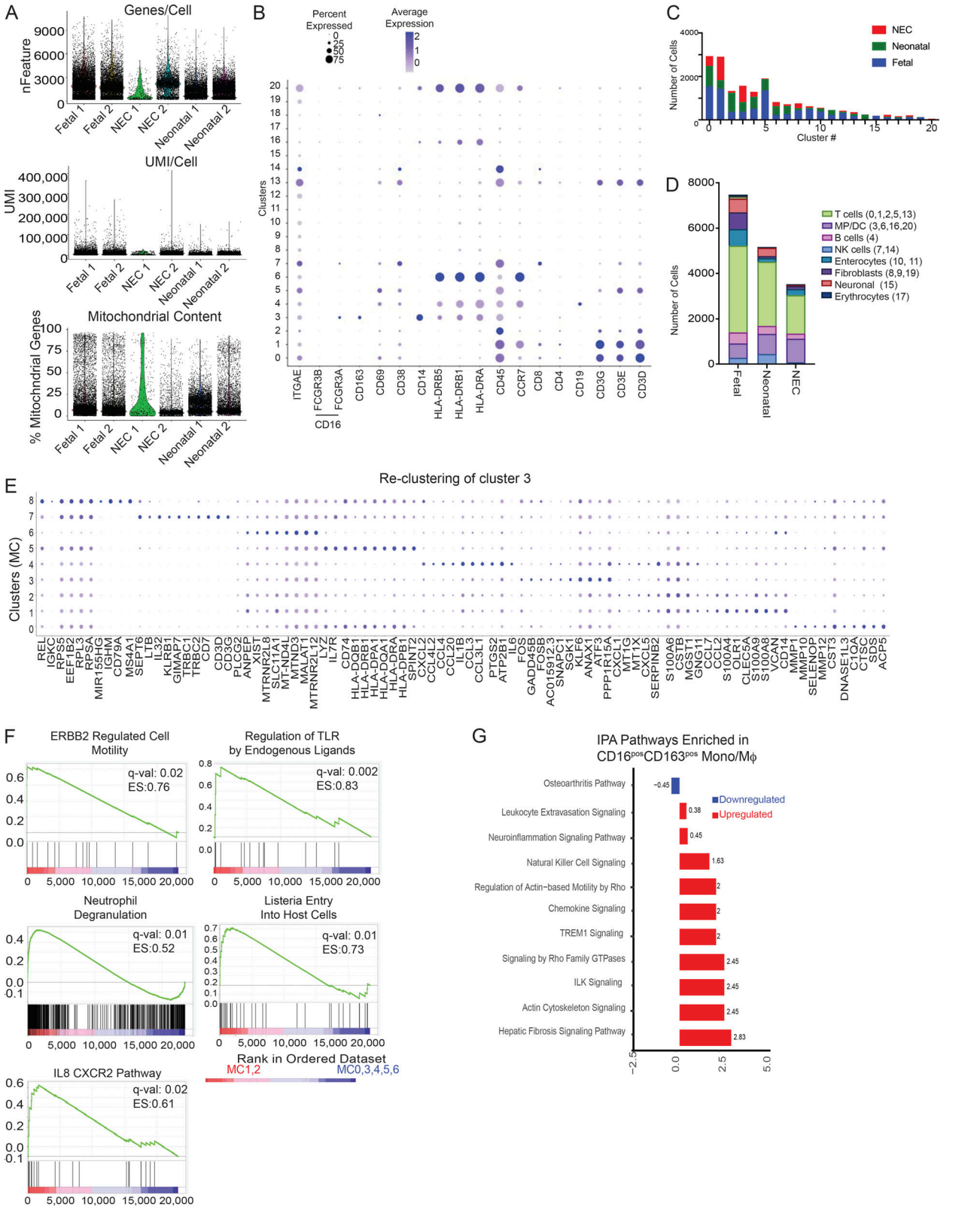

Figure S4. **Additional data from scRNA-seq experiments. (A)** Violin plot of genes per cell, unique molecular identifier (UMI)/cell, and mitochondrial content in each sample (NEC *n* = 2, one sample excluded from analysis for low cell number). **(B)** Average expression and percent expressed plot for genes used to identify clusters in Fig. 6 A and Fig. S5 D. **(C)** Median number of cells in each cluster colored by group. **(D)** Median number of cells per population (T cells, MP/DCs, B cells, NKT, enterocytes, fibroblasts, neuronal, and erythrocytes from Fig 6 A) in each group (fetal, *n* = 2; neonatal, *n* = 2; NEC, *n* = 1). **(E)** Average expression and percent expressed plot for top 10 genes in each cluster from reclustering of cells in cluster 3 from Fig 6 D. **(F)** Select GSEA pathways significantly enriched in MC1 and MC2 monocytes. **(G)** IPA pathways enriched in CD16^{+}CD163^{+} monocytes/Mϕ. ES, enrichment score.

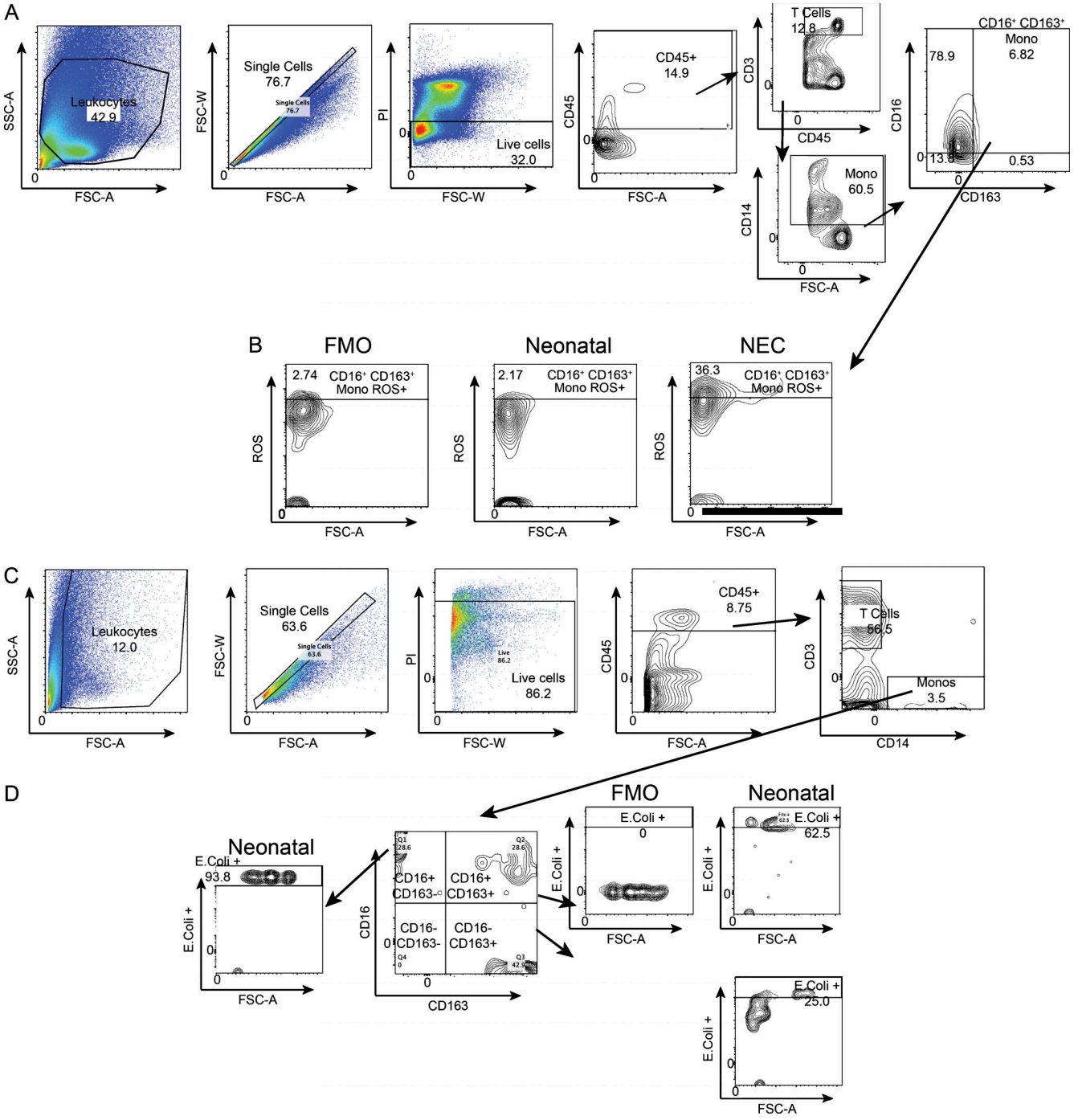

Figure S5. **Gating strategy for the flow cytometry experiments for ROS and bacterial uptake analysis. (A and B)** Gating strategy for measuring ROS generation by CD16^{+}CD163^{+} monocytes/Mϕ. **(C and D)** Gating strategy for bacterial uptake, measured by FITC-labeled *E. coli* uptake by subtypes of monocytes/Mϕ. FMO, fluorescence minus one; FSC-A, forward scatter area; FSC-W, forward scatter width; SSC-A, side scatter area.